CHARGED KAON PRODUCTION AT MID-RAPIDITY IN GOLD-GOLD COLLISIONS AT 130 GEV

A Thesis

Submitted to the Faculty

of

Purdue University

by

Alex Cardenas

In Partial Fulfillment of the

Requirements for the Degreee

of

Doctor of Philosophy

August 2002

To Chinto and Chela

ACKNOWLEDGMENTS

This dissertation represents more than the end of graduate school. It is also the culmination of over a decade of enrichment in the field of Physics which began in high school. I would like to thank every person who helped me reached this achievement. Thanks to my co-major professor Andrew Hirsch who was the first person ever to talk to me about the field of High Energy Nuclear Physics, as well as the STAR experiment. Thanks also to my other co-major professor Rolf Scharenberg, as well as professors Norbert Porile and Sergei Khlebnikov for serving in my advisory committee. A special thank you goes to Professor Fuqiang Wang for making me aware of the importance of charged kaon production, for guiding me in all aspects of data analysis, and for pushing me to try harder. Without his support this thesis could not have been completed. Thank you very much to Dr. Brijesh Srivastava for his advice on many issues that extended beyond Physics . Thanks to Dr. Blair Stringfellow for helping me get familiarized with the hardware component of the experiment. Also thanks to Dr. Eric Hjort for teaching me how to work with simulations. I would also like to thank Dr. Olga Barannikova whose computer expertise was a most valuable resource in this project. Without her I would have not been able to learn so much. Dr. Zubayer Ahammed was also of great help, especially on how to use LaTex to write this dissertation. My fellow graduate student Timothy Herston would answer some of my doubts as well as making the work place more interesting. The most junior members of our group, Brandon Parks, Jason Ulery, and Levente Molnar provided me with friendship which is appreciated. I also would like to thank other people, that even though are not part of the Purdue high energy nuclear physics group, played a big role in the completion of this thesis, one way or another. My former advisor from Worcester Polytechnic Institute, professor Padmanabhan K. Aravind always kept me motivated and whose advises I still seek many years later. My high school Physics teachers, Alicia Espinoza and Gonzalo Molina who are responsible for my decision to go into this field and supported it. Finally, thank you very much to a very special group of people: my family. To my parents Griselda and Dr. Jacinto Cardenas, for supporting my decision to major in Physics even though they did not agree with it. Also for supporting me financially during my undergraduate years, and above all for being a source of inspiration. To my siblings Ivan and Maria Eugenia, thank you for sacrificing material goods, so I could pursue my dreams. To all of you, thank you very much.

TABLE OF CONTENTS

LIST OF TABLES vii

LIST OF FIGURES viii

ABSTRACT xii

1 THEORY 1

1.1 Introduction 1
1.2 Quantum Chromodynamics 5
1.3 The Bag Model 11
1.4 Quark-Gluon Plasma 12
1.4.1 QGP at High Temperature 12
1.4.2 QGP at High Net Baryon Density 14
1.5 Heavy Ion Physics 18
1.6 Signatures of QGP 21
1.6.1 J/ψ Suppresion 21
1.6.2 Strangeness Enhancement 23
1.6.3 Chiral Symmetry Restoration 26
1.6.4 Other Probes 28
1.7 Gluon Saturation 29

2 EXPERIMENT 33

2.1 The Relativistic Heavy Ion Collider 33
2.2 The STAR Detector 37
2.3 Magnet 40
2.4 Time Projection Chamber 42
2.5 Silicon Vertex Tracker 49
2.6 Electromagnetic Calorimeter 49

2.7 Triggers . . . 51
2.8 Data Taking . . . 57
2.9 STAR Organization . . . 59

3 ANALYSIS . . . 61

3.1 Kaons . . . 61
3.2 Data Sample and Cuts . . . 63
3.3 Kaon Identification . . . 64
3.4 The z Variable . . . 67
3.5 Spectra . . . 68
3.6 Corrections for Efficiency . . . 75
3.7 Energy Loss Correction . . . 80

4 RESULTS . . . 86

4.1 Kaon Yields and Ratios . . . 86
4.2 Omega Variable . . . 92
4.3 Summary and Discussion . . . 97

BIBLIOGRAPHY . . . 101

VITA . . . 108

LIST OF TABLES

1 Quarks 9

2 Centrality bins definition 65

3 Energy loss dependence on the number of hits. As can be seen from the numbers, there is no dependence. 84

4 Summary of fitting results: Quoted errors are combined statistical and uncorrelated systematic errors; An additional 10% and 8% correlated systematic errors are estimated for dN/dy and T respectively. 88

LIST OF FIGURES

1 Energy density in lattice QCD for the 3 models described on the text. At the critical temperature there is a jump in energy density, indicating a phase transition. 10

2 Evolution of the early universe after the big bang. Hadronization occurs between 1 and 10 microseconds after the big bang. 15

3 Phase diagram of nuclear matter. The shaded area represents the boundary between hadron gas and the quark-gluon plasma. RHIC probes a region of higher temperature and lower net baryon density than SPS and AGS, which resembles more to the early universe. 17

4 Heavy ion collision. The two Lorentz contracted nuclei approach each other at near the speed of light. After colliding, the energy deposited in the vacuum will be enough to create particles that will expand in the fireball. 19

5 RHIC complex. The journey of the gold ions start at the Tandem Van de Graaff and ends at the RHIC ring. See text for details on each of the accelerators. 36

6 Cross sectional view of a RHIC magnet. The pipe in the middle is where the heavy ions travel. That pipe is only a few centimeters across. 38

7 Front view of the STAR detector showing several components as well as its relative size compared to a person. 41

8 Side view of the STAR detector showing most of the subsystems. 41

9 Diagram of the Time Projection Chamber showing the locations of the central membrane and the field cages. 44

10 Outer Field Cage: It is designed to allow particles pass through it but it must also be gas tight. 44

11 Inner Field Cage: Its properties are similar to those of the outer field cage. 45

12 Pads distribution in a TPC sector. The number of pads on each row can be seen to the right. 46

13 Drift velocity as a function of the electric field for several mixtures of argon and methane. The mixture used at STAR (P10) was chosen taking into account several issues explained on the text. 47

14 TPC software chain used for both simulations and data analysis. The description of each step is found on the text. 48

15 SVT: view perpendicular to the beam axis. 50

16 Front view of the EMC showing its relative position with respect other STAR components. 51

17 Side view of the EMC where the location of the endcap can be seen. . . . 52

18 Relative position of the trigger detectors at STAR. The CTB and the ZDC were the most important for our analysis. 53

19 View of the components of one of the trays that make up the CTB barrel. 54

20 Diagram of the composition of the ZDC. 55

21 Correlation between the ZDC and the CTB used to trigger centrality. Central collisions are located at the lower right corner. See text for details. 56

22 Trigger levels. See text for details on each level. 57

23 Comparison of DCA distribution between data (dark points) and MC (light points). For minimum bias they match as can be seen on the picture. The same comparison was made for different p_t cuts and different centrality bins and a match was found in all cases. 64

24 Comparison on the number of fit points from MC (points) with data (histogram) showing the agreement. 65

25 Energy loss (dE/dx) vs p: Particle identification in the TPC is achieved by the different energy loss rate of of different species of particles. Notice that the kaon band can be distinguished up to a momentum of about 0.6 GeV/c. 67

26 Energy loss in terms of the z variable. The kaon band is centered at z=0 which makes its identification easier once it is fitted to a gaussian. 68

27 Fitting of z to gaussians. Notice that the kaon gaussian is centered at z=0. The area under the gaussian is proportional to the yield. 69

28 Widths of the gaussians. Widths are required to obtain the area of the gaussian, and hence the yields. Crosses are pions, circles are kaons and filled squares are protons. Notice how kaons and pions are superimpossed above 0.5 GeV/c, while (anti)protons remain separate. See text for explanation. 71

29 Centroids of the four gaussians. This is basically the dE/dx. Notice the portion of the electron band fixed to take into account the effect of relativistic rise. See text for explanation. 72

30 Kaon centroid in terms of z. It is centered around zero based on the definition of z. 72

31 Raw spectra: circles are kaons, lines are electrons. At high p_t electrons are fixed to get rid of contamination to the kaons. 73

32 Ratio of raw spectra of electrons to raw spectra of kaon. Notice that in the region where they merge, at around 0.6 GeV/c, electrons contribute to the kaon peak by about 10%. 73

33 Corrected spectra. Kaons are fitted to an exponential in m_t as described on the text. The parameter p0 on the box represents the yield, while p1 is the inverse slope parameter. The circles are the electrons which yields are fixed at high p_t. 75

34 Comparison between data and MC of the electron yield where the agreement can be seen. Understanding the electron (positron) contamination is very important for our analysis for reasons described on the text. . . 76

35 Efficiency for K-. 77

36 Efficiency for K+. 78

37 Efficiencies ratio: this is the ratio of the previous two plots. The parameter p0 on the box is the value of the fitting function (solid line). Notice the 1% difference explained on the text. 79

38 Energy loss as a function of p_t for $|z| < 100$. 81

39 Energy loss as a function of z vertex. See text for an explanation of the three regions and how they were used to determine the z vertex cut. 81

40 Energy loss as a function of p_t for $|z| < 30$. 82

41 Energy loss as a function of p_t for $Nhits > 15$. 83

42 Energy loss as a function of p_t for $Nhits > 35$. 84

43 Comparison of the energy loss for different number of hits. There is no difference between them as can be seen on the numbers on table 3. . . . 85

44 Charged kaon invariant yield tranverse mass spectra for selected centrality bins. Solid lines correspond to fitting to an exponential in m_t. Error bars are statistical. See text for description on systematic errors. 88

45 Centrality dependence: (a) of kaon inverse slope parameter and (b) the kaon to negative hadron ratio. Kink results are also shown to demonstrate agreement between two methods. 91

46 Energy dependence of (a) K/π ratios and (b) K^+/K^-. The curves on (a) are parametrization to p+p data. Also on (a), systematic errors of the STAR data are indicated by caps. See text for explanation. 93

47 K^-/π vs ω: Notice how data from previous experiments increase linearly while STAR data points saturate. Possible explanations of this phenomenon are described on the text. 96

ABSTRACT

Cardenas, Alex. Ph.D., Purdue University, August, 2002. Charged Kaon Production at Mid-Rapidity in Gold-Gold Collisions at 130 GeV. Major Professors: Andrew Hirsch and Rolf Scharenberg.

We report results of charged kaon production at mid-rapidity in Au+Au collisions at $\sqrt{s_{NN}} = 130$ GeV measured by the STAR experiment at RHIC. The yields are described by an exponential in tranverse mass. The inverse slope parameter shows a slight increase with centrality. The K^-/π^- and K^+/π^+ ratios are constant across centrality, and they are enhanced by about 50% with respect to p+p and p+$\bar{p}$ collisions at the same energy. The negative kaon to pion ratio as a function of a new experimental variable called ω seems to saturate at RHIC which might be indication of gluon saturation.

1 THEORY

1.1 Introduction

The search for the ultimate bulding blocks of matter can trace its origin to ancient Greece where the atomists of the fifth century B.C., Leucippus of Miletus and Democritus of Abdera suggested that the world consisted of an infinity of tiny atoms moving randomly in an infinite void. These atoms were solid corpuscles of many shapes, immutable, colliding with each other, and no alteration of them was possible [1]. This idea remained buried through the middle ages until it was resurrected by Pierre Gassendi in the XVII century when he also suggested indivisible atoms filling the void make up all matter. However it was not until the XVIII century, when the concept of atom as we know it today became part of modern science. First, Robert Boyle on his book "The skeptical chemist", proposed the idea that matter consists of atoms in motion and all physical and chemical phenomena can be explained as the results of collisions among atoms. Soon after that, Antoine Lavoisier published his book "New system of chemistry" where he introduced the ideas of indestructibility and conservation of matter which he explained with the concept of atoms. The atomic theory, as ultimate building blocks of matter, came to existence in the XIX century with John Dalton. On his book "A new system of chemical philosophy", he established some of the rules of physics and chemistry still in use today such as all matter is made up of atoms, they are the same for a given element and different from atoms of other elements [2]. At the end of the XIX century, with the successful predictions of the periodic table, it seemed as scientists had found in the atom the most basic unit of matter. All that changed in 1896 when Henry Becquerel discovered radioactivity and in 1897 when J.J. Thomson discovered the electron. It was obvious then, that atoms were made up of even more fundamental particles. In 1911, Ernest Rutherford discovered the nucleus of the atom, and developed the nuclear atom model: atoms consist of a nucleus with electrons orbiting around it. The only problem this model had was its failure to predict the mass of certain atoms in term of protons and electrons only, but this problem was solved in 1932 by James Chadwick when he discovered the neutron. Once again scientists thought the structure of matter was completely understood in terms of protons, neutrons and electrons, and once again they were wrong. Nuclear physicists had the task to explain how electrically neutral neutrons could bind together in the nucleus, and what it was even more difficult, how positively charged protons did not repel each other. It was proposed that a new type of interaction, one stronger than the electromagnetic force, was responsible for the stability of nuclei. This interaction was called the strong force, and the first significant theory of it was developed by Hideki Yukawa in 1934. He proposed that nucleons interact with each other via the exchange of a new particle called meson (pion) which was later discovered by Cecil Powell in 1947. The picture became more complicated after the discovery of the neutral kaon (1947) and the charged kaons (1949) followed by many more strongly interacting particles (hadrons) during the 1950's. In 1964, Gell-Mann and Zweig independently suggested that hadrons are not fundamental particles [3]. Instead they are composed of even more elementary constituents called quarks. The quark model was able to explain the variety of hadrons observed experimentally, but individual quarks were never observed. They seemed to be always confined within hadrons, interacting with each other via the exchange of a group of particles called gluons. During the 1970's a theory of strong interactions was developed to explain all known properties of quarks and gluons. This theory is known as Quantum Chromodynamics or QCD for short. Among other things QCD predicts that at very high energy densities, such as those that existed in the very early universe (a few microseconds after the Big Bang), hadronic matter undergoes a phase transition into a state of nuclear matter called the quark-gluon plasma (QGP). Put in simple words, QGP occurs when hadrons "melt" into quarks and gluons, which are then free to roam inside the nuclear volume. In order to study QGP we would need to recreate such high energy density conditions in the laboratory. The only method we have available to do that is through the collisions of ultrarelativistic nuclei. During the 1980's and 1990's, experiments with this objective were performed at the Alternating Gradient Synchrotron (AGS) and at the Super Proton Synchrotron (SPS). In spite of some circumstancial evidence of QGP, no smoking gun was found at these experiments. We are now at the dawn of the XXI century, and the search for the building blocks of matter continues.

A new era in this search began in June 2000, when the Relativistic Heavy Ion Collider (RHIC) at Brookhaven National Laboratory (BNL) provided the first head on collisions of ultrarelativistic gold nuclei at the highest energies to date of 130 GeV per nucleon pair. The Purdue High Energy Nuclear Physics group is a member of the Solenoidal Tracker At RHIC (STAR) collaboration, one of the four experiments searching for QGP. If QGP is formed, there would be several signals or signatures that could be observed. One of these signatures would be an increase in the production of strange particles with respect to a non-QGP scenario. The lowest mass strange particle is known as kaon, therefore of all strange particles, kaons would be the most easily produced. Since kaons carry most of the strangeness produced in heavy ion collisions, we have chosen to study them to seek for strangeness enhacenment. This enhancement can be observed in the ratio of kaons with respect a non-strange particles such as pions. The first goal of this thesis is to study the charged kaon production at the STAR detector and compare it with previous experiments to see if there is a strangeness enhacement. In addition, a second goal of this dissertation is to study the phenomenon of gluon saturation to try to understand the initial conditions of the fireball through the introduction of a new experimental variable called ω.

In this project we present the analytical tools behind the study of the charged kaon production at RHIC. For that purpose this dissertation is divided into 4 chapters or sections. This first section presents a brief introduction to QCD, the theory behind QGP, and how the STAR experiment can shed light on it. It also deals with Heavy Ion Physics in general, describing some of the accelerators that have been and will be involved in this field, as well as the other experiments from RHIC. In this section we also describe some of the expected signatures of QGP in heavy ion collisions as well as the theoretical motivation behind gluon saturation. Section 2 gives a description of the experimental equipment we used: RHIC and the STAR detector with some of its subsystems. Section 3 presents our method of analysis. We start section 3 by describing how we selected the data that was analyzed, the type of corrections that needed to be made and the procedure used to obtain results. We conclude this dissertation discussing the results in chapter 4. We describe our results in terms of the common parameters that have been used by previous experiments, such as collision centrality and energy. These type of studies are well established and make our results and previous publications easy to compare. At the end of the chapter 4, we study the charged kaon production as a function of our new variable ω and we suggest that it might be related to gluon saturation and we argue that it should be studied further.

1.2 Quantum Chromodynamics

As mentioned in the introduction, Quantum Chromodynamics (QCD) is the theory of strong interactions. It was developed to explain how at the fundamental level, quarks and gluons interact with each other, and at a residual level, how hadrons interact with each other. It's lagrangian has the following form [3]:

$$L = [i\hbar c\bar{\psi}\gamma^{\mu}\partial_{\mu}\psi - mc^2\bar{\psi}\psi] - \frac{F^{\mu\nu} \cdot F_{\mu\nu}}{16\pi} - (q\bar{\psi}\gamma^{\mu}\lambda\psi) \cdot A_{\mu} \quad (1)$$

Just as in Quantum Electrodynamics (QED) where fermions (leptons) interact by exchanging bosons (photons), in QCD fermions (quarks) also interact via the exchange of bosons (gluons). There are six flavors of quarks divided in 3 generations. The first generation are the up (u) and down (d) quarks. The second generation are the strange (s) and charm (c) quarks. The third generation are the top (t) and bottom (b) quarks. Each one of these quarks has its respective anti-quarks. The second and third generations are replicas of the first one but more massives. However these flavors are irrelevant in QCD because, as in QED, mass is not distinguished by the strong interaction. QCD cares only about another propery of the quarks, called the color charge which is analogous to the electric charge in QED. But unlike QED where there are only 2 varieties of charge (positive and negative), in QCD we have 3 different colors with their respective anticolors, for a total of 6 different possibilities. They are red, antired, blue, antiblue, green and antigreen. It has been established that each quark carries color and each anti-quark carries a unit of anticolor. A very important difference between QED and QCD is the fact that while in QED photons don't carry electric charge, in QCD gluons carry color. Each gluon carries 1 unit of color and 1 of anticolor. Naively speaking, this would imply 9 different gluons: $r\bar{r}$, $b\bar{b}$, $g\bar{g}$, $r\bar{b}$, $r\bar{g}$, $b\bar{r}$, $b\bar{g}$, $g\bar{r}$, and $g\bar{b}$. However this is not the case. Instead, gluons exists in a superposition of color states, and we only have 8 gluons given by:

$|1> = (r\bar{b} + b\bar{r})/\sqrt{2}$

$|2> = -i(r\bar{b} - b\bar{r})/\sqrt{2}$

$|3> = (r\bar{r} - b\bar{b})/\sqrt{2}$

$|4> = (r\bar{g} + g\bar{r})/\sqrt{2}$

$|5> = -i(r\bar{g} - g\bar{r})/\sqrt{2}$

$|6>=(b\bar{g}+g\bar{b})/\sqrt{2}$

$|7>=-i(b\bar{g}-g\bar{b})/\sqrt{2}$

$|8>=(r\bar{r}+b\bar{b}-2g\bar{g})/\sqrt{6}$

These 8 states form a color octet. The ninth state:

$|9>=(r\bar{r}+b\bar{b}+g\bar{g})/\sqrt{3}$

constitute a color singlet which is excluded by experimental observation as follows: In general, the potential of an interaction is given by Yukawa's potential:

$$V(r)=\frac{exp(-\mu r)}{r} \tag{2}$$

where μ is proportional to the mass of the boson which carries the interaction. Gluons, being massless, mediate a force of infinite range, while pions being massive have a limited range. A singlet state such as a proton or a neutron can only emit and absorb a singlet (a pion or the ninth gluon). If the ninth gluon existed, it could be exchanged between nucleons and that would give rise to a infinite range strong interaction, just like the electromagnetic interaction. However the strong interaction is short range which means that it is a virtual pion and not a gluon what is exchanged between nucleons. This behavior of the strong force is known as "residual" strong interaction.

Since gluons carry color they are therefore able to interact among themselves unlike photons in QED. These gluon-gluon interactions give rise to a running coupling constant with the following form [3]:

$$\alpha_s(|q^2|)=\frac{\alpha_0}{1+\frac{\alpha_0}{12\pi}(11n-2f)ln\frac{|q^2|}{\mu^2}} \tag{3}$$

where α_0 is the coupling constant for momentum transfer q, μ is a scale constant which must satisfy $\mu \ll q$, n is the number of colors (3) and f is the number of flavors (6). Another way to express the coupling constant is as:

$$g_s = \sqrt{4\pi\alpha_s} \tag{4}$$

which will be used later. We can also define a new variable called Λ_{QCD} as:

$$ln\Lambda_{QCD}^2 = ln\mu^2 - 12\pi/[(11n - 2f)\alpha_s] \tag{5}$$

which is just a parameter that will be useful when studying gluon saturation.

From equation (3) it can be noticed that at low momenta, or long distances, the coupling constant increases. Thus the energy that is put into separating 2 quarks will be enough to create another quark-antiquark pair that will bound to the original pair. This effect is called quark confinement. Because of confinement, quarks form colorless clusters. These clusters are either a quark-antiquark pair (mesons) or a 3 quark system (baryons). Mesons and baryons form the family of strongly interacting particles which are called hadrons. Mathematically, hadrons can be better understood in terms of the potential describing quarks interactions. For mesons, this potential is given by [4]:

$$V(r) = -\frac{A(r)}{r} + Kr \tag{6}$$

where A(r) is given by:

$$A(r) \propto \frac{1}{ln(1/r)} \tag{7}$$

and K is a constant called the "string tension" whose value is around 880 MeV/fm. This value is obtained by matching the mass of the hadrons with their angular momentum. At very small distances, the first term of equation (6) takes over, and the

Table 1: Quarks

Flavor	Charge (e)	Current Mass (GeV)	Constituent Mass (GeV)
up	+2/3	0.004	0.35
down	-1/3	0.007	0.35
charm	+2/3	1.5	1.5
strange	-1/3	0.15	0.55
top	+2/3	175	175
bottom	-1/3	4.7	4.7

interaction between quarks gets weaker when they get closer to each other. In the limit $r \to 0$ quarks interact very weakly with each other behaving almost like free particles. This property is called asymptotic freedom. On the other hand, if we increase the separation between quarks, the second term of equation (6) takes over, and the potential increases linearly with distance. Therefore the force between a quark-antiquark pair does not decrease with distance. This is another way to explain the confinement effect mentioned above. Quark confinement and asymptotic freedom are 2 important characteristics of hadronic matter that are addressed in the bag model which will be explained in section 1.3.

Since QCD is a mathematically challenging theory whose exact solutions are difficult to obtain, a big part of what we know about it is obtained numerically. This method employs calculations on a lattice that discretizes space-time, therefore is called lattice QCD[5-8]. This method is used among other things to estimate the transition temperature from QGP to hadronic gas, as well as the energy density dependence on

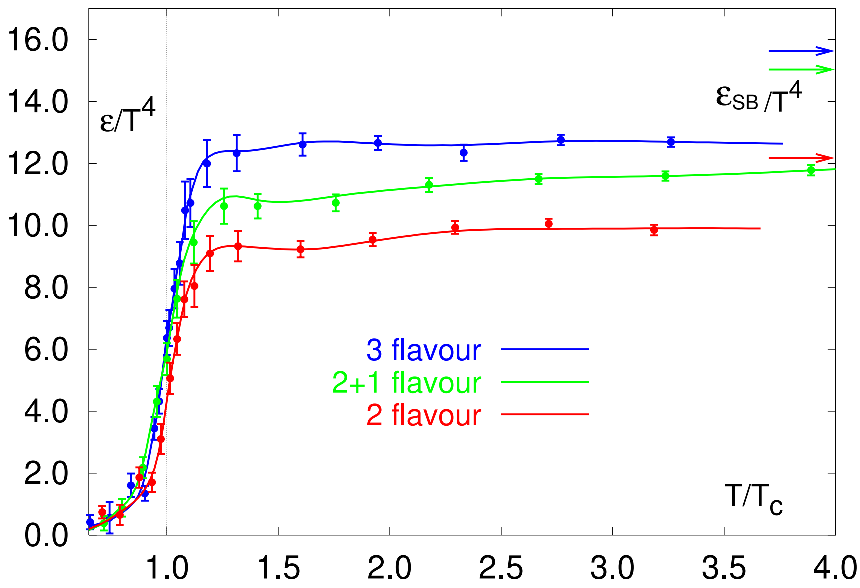

Figure 1: Energy density in lattice QCD for the 3 models described on the text. At the critical temperature there is a jump in energy density, indicating a phase transition.

temperature. Calculations have been performed in 3 different models: 2-flavor QCD (with 2 light quarks), (2+1)-flavor QCD (2 light quarks and 1 heavy quark), and 3-flavor QCD (3 light quarks). These calculations give an estimate for the transition temperature of 175 MeV for the 2 and 2+1 flavor QCD, and 155 MeV for the 3 flavor QCD. The energy density dependence on temperature has also been studied in these 3 models. Figure (1) shows the result. This figure can also be interpreted as the number of degrees of freedom versus temperature. Notice in the picture how there is a sudden jump in the energy density with respect temperature. That is the phase transition we are looking for. Calculations estimate that the phase transition occurs at an energy density approximately equal to $2.5GeV/fm^3$. In section 1.4 we will go into more details about QGP.

1.3 The Bag Model

From the description given above, hadrons can be described phenomenologically as massless quarks moving freely inside a bag. This is the so-called MIT bag model. This model was introduced to explain non-pertubative effects of QCD. In this model, the kinetic energy of the quarks creates an outward pressure. To keep the quarks from flying apart, the bag model introduces an external bag pressure, B, pushing inward. This bag pressure reproduces confinement. To obtain an estimate for B, it's necessary to solve the Dirac equation for a massless fermion in a cavity of radius R (hadrons). A detailed calculation can be found in reference [9], but the upshot is that the energy of a system of N quarks, confined in a bag of radius R is:

$$E = \frac{2.04N}{R} + \frac{4\pi R^3 B}{3} \tag{8}$$

We notice in this equation, that in the first term, the energy decreases with increasing radius, while the opposite is true according to the second term. Therefore there must be an equilibrium radius of this system which occurs at dE/dR = 0, which leads to the following result for the bag pressure constant:

$$B^{\frac{1}{4}} = \left(\frac{2.04N}{4\pi}\right)^{1/4} \frac{1}{R}. \tag{9}$$

1.4 Quark-Gluon Plasma

In the bag model, if the internal pressure of the quarks is greater than the external bag pressure B, the bag won't be able to confine the quarks anymore. The result is a state of deconfinement of quarks and gluons, called the quark-gluon plasma (QGP). In QGP, there would not be a definitive hadron boundary anymore, and quarks and gluons would be free to roam within the entire nuclear volume. The conditions necessary to create QGP can be obtained through two mechanisms: increase in temperature and/or increase in net baryon number.

1.4.1 QGP at High Temperature

To be able to easily estimate the transition temperature at which hadronic matter becomes QGP, it's necessary to assume that quarks and gluons are not interacting. Also, the number of quarks is equal to the number of antiquarks. It's found in reference [9] that the energy of a system of quarks is

$$E_q = \frac{7}{8} g V \frac{\pi^2}{30} T^4 \tag{10}$$

where V is the volume, T the temperature and g the degeneracy of quarks. The same equation applies for antiquarks. For gluons, the energy is given by

$$E = g_g V \frac{\pi^2}{30} T^4 \tag{11}$$

where g_g is the degeneracy of gluons. From statistical mechanics, for massless fermions and bosons:

$$P = \frac{1}{3}\frac{E}{V} = \frac{1}{3}\epsilon \tag{12}$$

where ϵ is the energy density. Therefore the pressure for a gas of massless quarks is

$$P = \frac{7}{8} g V \frac{\pi^2}{90} T^4 \tag{13}$$

which is the same for antiquarks. For gluons the pressure is given by

$$P = g_g V \frac{\pi^2}{90} T^4. \tag{14}$$

The contribution of quarks, antiquarks and gluons add to obtain the total pressure of QGP:

$$P = g_{qgp} \frac{\pi^2}{90} T^4 \tag{15}$$

where $g_{qgp} = (g_g + 7/8(g + \bar{g}))$. For g there are 2 flavors (up and down), 3 colors and 2 possible spins. That gives g=12. Same applies for $\bar{g}$. For g_g there are 8 gluons with 2 possible polarizations. That gives $g_g = 16$. So $g_{qgp} = 37$. Therefore, the pressure of QGP is then:

$$P = 37 \frac{\pi^2}{90} T^4 \tag{16}$$

and the energy density is:

$$\epsilon = 37 \frac{\pi^2}{30} T^4. \tag{17}$$

Dividing equation (17) by T^4, we obtain again the number of degrees of freedom discussed in section 1.2, and from figure (1) we see that at the transition the value jumps from 3 (hadronic gas) to around 12. Since pressure in QGP is related to temperature by equation (16) the transition from hadronic gas to QGP occurs at the critical temperature T_c where the pressure equals the bag pressure B. The critical temperature is then given by:

$$T_c = \left(\frac{90}{37\pi^2} \right)^{1/4} B^{1/4}. \tag{18}$$

At this point, some numerical values can be estimated. In a baryon we have 3 quarks confined to a distance of about 0.8 fm. Plugging in these numbers into equation (9) the value of the bag pressure constant is about 200 MeV. Plugging this value into equation (18) gives a critical temperature of around 140 MeV, which is close to that obtained from lattice QCD (see section 1.2). Equation (17) can be used to estimate energy density. For T = 200 MeV ϵ is near $2.5GeV/fm^3$ which is the same value obtained in lattice QCD (see previous section) . This values of temperature and energy density are similar to those found in the early universe, between 1 and 10 microseconds after the Big Bang (see figure 2). Therefore studying QGP may also have important cosmological applications because it could shed light on the inital moments of the universe and help us answer some fundamental questions such as how matter was formed.

1.4.2 QGP at High Net Baryon Density

Even if T=0 it is still possible to create QGP. Consider a case where the number of quarks inside the bag is high. Pauli's exclusion principle will make some of those quarks populate states of higher momentum. This will lead to an increase in the internal pressure of the quark gas. When this pressure exceeds the external bag pressure, deconfinement will occur. Since each quark has a baryon number of 1/3, high quark density will be equivalent to high baryon density. To estimate this density it is necessary to start with the number of quarks in the bag and the energy of the quark gas [9]:

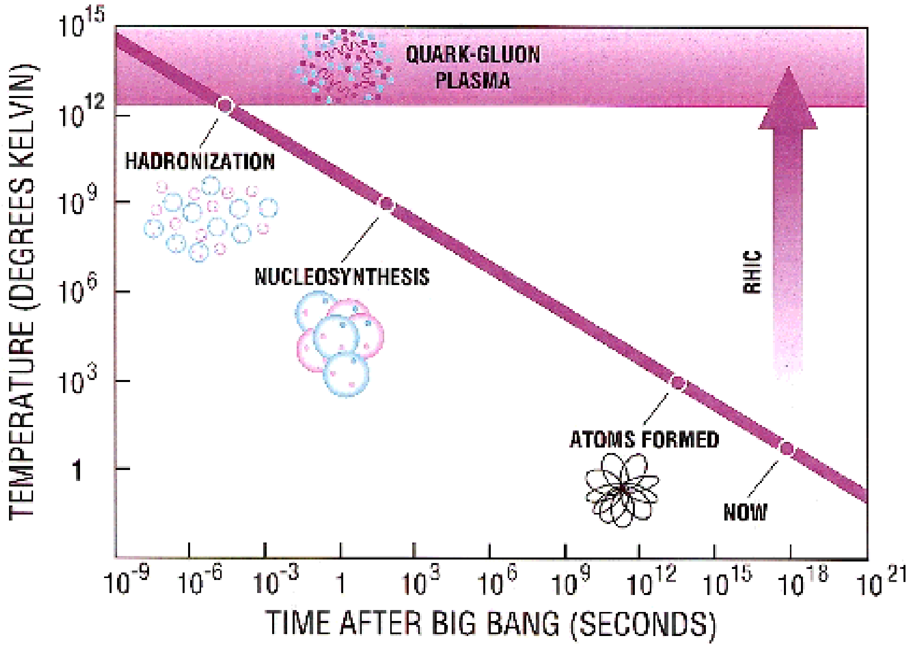

Figure 2: Evolution of the early universe after the big bang. Hadronization occurs between 1 and 10 microseconds after the big bang.

$$N_q = \frac{gV\mu^3}{6\pi^2} \tag{19}$$

$$E_q = \frac{gV\mu^4}{8\pi^2} \tag{20}$$

where μ is the fermi momentum. Dividing these 2 equations by volume we obtain the number density and the energy density of the quark gas:

$$n_q = \frac{g\mu^3}{6\pi^2} \tag{21}$$

$$\epsilon_q = \frac{g\mu^4}{8\pi^2} \tag{22}$$

Since $P = (1/3)\epsilon$ and the deconfinement condition is P=B, we obtain an expression for the fermi momentum μ :

$$\mu = \left(\frac{24\pi^2 B}{g}\right)^{1/4} \tag{23}$$

This value of μ can be plugged into the expression for n_q equation (21). Dividing it by 3 gives us the baryon number density:

$$n_B = \frac{4}{3}\left(\frac{g}{24\pi^2}\right)^{1/4} B^{3/4} \tag{24}$$

The degeneracy g of ordinary nuclear matter is 3 colors x 2 spins x 2 flavors = 12. This gives $n_B = 0.72/fm^3$. For comparison, we calculate now the baryon density of ordinary nuclear matter. It is just the number of nucleons (A) per unit volume ($4\pi r^3/3$). The radius of the nucleus has been empirically determined to be proportional to $A^{1/3}$ times a constant value of 1.12 fm. Therefore

$$n = \frac{A}{\frac{4\pi}{3}((1.12fm)A^{1/3})^3} = \frac{1}{\frac{4\pi}{3}(1.12fm)^3} = 0.17/fm^3 \tag{25}$$

Therefore n_B is about 5 times the density of ordinary nuclear matter. Other estimates place this value between 5 and 10 times the nuclear density. This is the type of condition that is thought to exist in the interior of neutron stars. Even more exciting, recently, scientists combining data from the Chandra X-ray observatory and the Hubble Space Telescope have discovered stars that they think may be made of quark matter. They have a density between those of neutron stars and black holes. If confirmed, this discovery would make the astrophysical applications of studying QGP even more important.

We have analyzed the two extreme cases: T=0 with high net baryon density, and 0 net baryon density with high temperature. It's obvious that in between those two

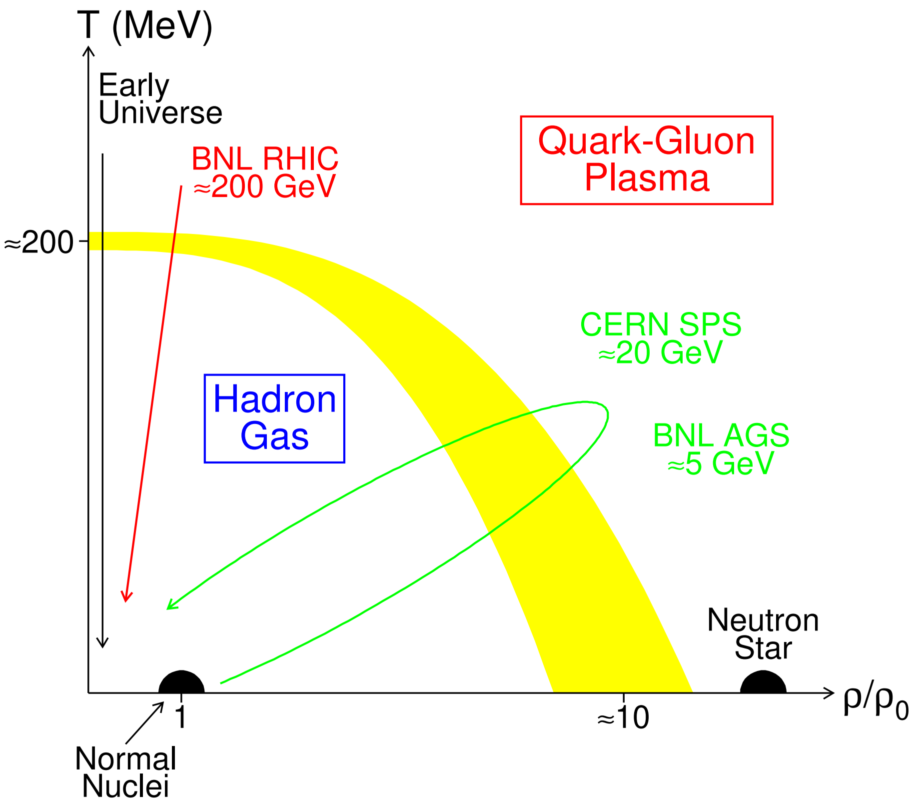

Figure 3: Phase diagram of nuclear matter. The shaded area represents the boundary between hadron gas and the quark-gluon plasma. RHIC probes a region of higher temperature and lower net baryon density than SPS and AGS, which resembles more to the early universe.

extremes there are also other combinations of temperature and net baryon density that give rise to QGP. If we plot temperature versus net baryon number we obtain the phase diagram of nuclear matter. There it is possible to see the boundary between hadronic matter and QGP for all T and n_B(see figure 3).

1.5 Heavy Ion Physics

The only method we have available to create QGP is through ultrarelativistic heavy ion collisions[10-12]. In the center of mass system of the colliding nuclei they look flat, like pancakes, because of Lorentz contraction (see figure 4). These colliding nuclei will deposit a fraction of their kinetic energy into a tiny region of space. The term nuclear stopping power refers to the degree of stopping which a nucleus suffers when it collides with another nucleus. The amount of nuclear stopping power determines basic parameters such as energy and volume of the interaction region which govern the reaction dynamic. The interaction region consists of an excited vacuum. This excited vacuum may have an energy density high enough to create QGP. After its creation, QGP will expand and cool down very quickly, leading to hadronization at around $10^{-23}s$. Therefore QGP can't be observed directly. But particles coming out of the fireball will hopefully carry enough information about the initial state to determine if QGP was indeed formed. Possible signatures will be described later.

In order to better understand relativistic heavy ion collisions, we must know some of the terminology used to describe them. Below we define a few variables that will be found later in this dissertation. They are:

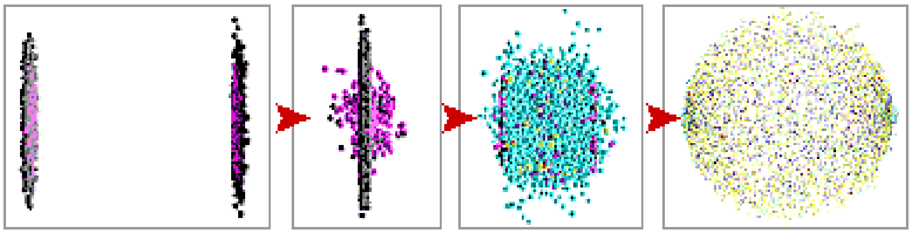

Figure 4: Heavy ion collision. The two Lorentz contracted nuclei approach each other at near the speed of light. After colliding, the energy deposited in the vacuum will be enough to create particles that will expand in the fireball.

•p_z, longitudinal momentum, is the component of the momentum in the beam direction. It is also known as p_L.

•p_t, transverse momentum, is the component of the momentum perpendicular to the beam direction.

•$\sqrt{s}$ is the energy in the center of mass. The variable s itself is one of the Mandelstam variables defined as $s = (p_A + p_B)^2$ where p_A and p_B are the 4-momenta of the colliding particles.

•y is the rapidity of a particle, defined as:

$$y = \frac{1}{2} ln \frac{E + p_z}{E - p_z} \tag{26}$$

•m_t is the tranverse mass, defined as:

$$m_t = \sqrt{m^2 + p_t^2} \tag{27}$$

where m is the rest mass of the particle.

•η is the pseudorapidity of a particle and it's defined as:

$$\eta = \frac{1}{2} ln \frac{|p| + p_z}{|p| - p_z} = -ln(tan\frac{\theta}{2}) \tag{28}$$

where θ is the angle of emission of the particle with respect to the beam direction. The pseudorapidity η is a very convenient variable because it can be measured without knowing the momentum of the particle.

Now that we have a definition of the terms used, let us explain what happens in the reaction in a little more detail. The Lorentz contracted nuclei meet in inelastic collisions, superimposing themselves creating a high density zone. The released partons from this collisions rescatter several times. This results in their momenta, which were initially correlated along the beam axis, being redistributed and a substantial fraction of the kinetic energy being deposited in the mid-rapidity region (y=0). As mentioned above, this energy creates quarks and antiquarks which bind together to form hadrons. The way these quark-antiquark pairs are created can be understood in terms of "strings". Once the energy density in the fireball drops near transition, the color field between the partons form "flux tubes" or "strings" which have a thickness of about 1 fm and a energy length density (or string tension) of about 880 MeV/fm (see section 1.2). This string network expands and the energy is then transformed into quarks and antiquarks.

The energy density in the fireball is given by:

$$\epsilon = \frac{m_T}{\tau A}\frac{dN}{dy} \approx \frac{N}{A}\frac{d < E >}{2tdy} \tag{29}$$

where τ is the proper time after the collision. When the temperature in the fireball drops under the transition temperature, the hadrons are formed and we have chemical freeze out. This hadronic gas cools until interaction rates become insufficient to maintain thermal equilibrium. This point is known as thermal freeze out. The information we have from the fireball comes from the surface of last scattering at thermal freeze out.

1.6 Signatures of QGP

As mentioned earlier, a QGP is not directly observable because it exists only for a short period of time. What is observable are the hadronic and leptonic residues of the plasma phase. Leptonic probes provide information about the spectrum of electromagnetic current fluctuations in the QGP, while hadronic probes carry information on the quark flavor dynamics. The problem with each of these probes is that they are indirect signals. Therefore the experiments are focused on observing as many of them as possible. Some of these QGP signatures [13-24] are described in the following sections:

1.6.1 J/ψ Suppresion

In QGP, a quark is surrounded by other quarks, antiquarks and gluons. As a consequence, the effective color charge of a quark will be reduced. This effect is called Debye screening. Debye screening makes the attractive force between c and $\bar{c}$ weak in QGP. Thus in QGP, c and $\bar{c}$ are more likely to fly apart than to bind. Also, inside QGP, the production of charm quark-antiquark pairs is reduced by a factor proportional to $exp(-m_c/T) = 6 * 10^{-4}$ relative to non QGP producing reactions, where m_c is the mass of the charm quark and T is the transition temperature. Thus chances that a c quark will find a corresponding $\bar{c}$ antiquark to bind are very slim. Consequently the production of J/ψ is suppresed compared to its production in a purely hadronic environment. In a little more detail, we have that the potential between 2 colored quarks is screened as $V = V_0 exp(-r/r_D)$ where r is the separation between the quarks, r_D is the Debye radius which depends on temperature, and V_0 is the Coulomb part of the potential. Once the hadron radius is greater than the Debye radius, deconfinement has occured. Lattice calculations predict that these two radii are roughly equal when the temperature is about 1.2 times the transition temperature. When the system expands and cools down to the hadronization temperature, the separation between c and $\bar{c}$ will be too large for them to form J/ψ. Let us use some numbers to try to understand quantitatively this effect. The radius of a J/ψ in vaccum is roughly $r_{J/\psi} = 0.45fm$ and its measured momentum is typically around $p = 0.67GeV/c$. The formation time of J/ψ in its own rest frame is then given by:

$$\tau = m_c r_{J/\psi}/p = 0.9fm/c \tag{30}$$

which transformed into the laboratory frame would be:

$$t = \tau[1 + (p^2/M^2_{J/\psi})]^{1/2} \tag{31}$$

where $M_{J/\psi}$ is the mass of the J/ψ. During this time, the c and $\bar{c}$ pair will move a distance away from its formation point given by:

$$r = \tau(|p|/M). \tag{32}$$

If t is larger than the lifetime of the plasma and r is larger than the radius of the QGP bubble, then J/ψ would survive. However this would imply a QGP that cools down very fast, much faster than predicted by any model. As a consequence we expect to observe J/ψ suppresion. For this very same reason, those c quarks which fail to bind with a $\bar{c}$, will now bind to a $\bar{u}$ or $\bar{d}$, thus creating other particles with so-called open charm. Thus there will be an enhancement in the number of open charm particles coming out of the collision, concurrent with a suppression of J/ψ production. This would constitute two affirmative signals of QGP formation.

1.6.2 Strangeness Enhancement

Another signature that has been suggested [25-28] as a probe of QGP is strangeness enhancement. In the hadronic scenario, the production of particles containing strange quarks is suppressed as compared with the production of particles containing the up and down quarks. This is due to the higher mass of the strange quark. Mathematically, the density of quarks in heavy ion collisions is given by:

$$n_q = \frac{g}{(2\pi)^3} \int \frac{d^3p}{exp[((p^2 + m_q^2)^{1/2} + \mu)/T] + 1} \tag{33}$$

For the up and down quarks, g = 2 flavors X 3 colors X 2 spins =12, and since they are light quarks their mass is approximately equal to zero. Therefore the equation for up and down quarks is reduced to:

$$n = \frac{12}{(2\pi)^3} \int \frac{d^3p}{exp[(p + \mu)/T] + 1} \tag{34}$$

while for the strange quarks, g = 1 flavor X 3 colors X 2 spins = 6, and their chemical potential is approximately equal to zero (see below). Therfore the equation for strange quarks is:

$$n_s = \frac{6}{(2\pi)^3} \int \frac{d^3p}{exp[(p^2+m_s^2)^{1/2}/T]+1} \tag{35}$$

where the m_s on the latter equation represents the strange quark mass. In a hadronic gas, n_s would be suppresed because of the large value of m_s(150 MeV) in the denominator. However we notice that near the transition temperature, the exponential term in the latter equation will not be as large as it is at low temperatures, therefore n_s would not be as suppresed. Also in QGP, gluon-gluon reactions are predicted to form a large number of s-$\bar{s}$ pairs. Mathematically this is observed in the cross-section for the two types of reactions that can lead to s-$\bar{s}$ pair production: quark-antiquark annihilation or gluon-gluon interaction respectively:

$$\sigma_{quark} = (8\pi\alpha_s^2/27s)(1+2m_s^2/s)W(s) \tag{36}$$

and

$$\sigma_{gluon} = \frac{2\pi\alpha_s^2}{3s}[(1+4m_s^2/s+m_s^4/s^2)tanh^{-1} - (\frac{7}{8}+\frac{31m_s^2}{8s})]W(s) \tag{37}$$

where $s = -(k_1+k_2)^2$is the invariant squared mass with k_1 and k_2 as the four-momenta of the colliding particles, and $W(s) = (1-4m_s^2/s)^{1/2}$. These additional gluon-gluon interactions will lead to an increase in the production of strange particles. Of course we have to check that all these s-$\bar{s}$ pairs produced in the QGP will not annihilate with each other before they have time to hadronize into strange particles. We need to estimate the strange quark density in the QGP taking into account both the production as well as the annihilation processes. The evolution of strange quark density ρ_s is given by:

$$d\rho_s/dt = A[1-(\rho_s/\rho_s^{\infty})^2] - (\rho_s/V)dV/dt \tag{38}$$

where ρ_s^∞ is the saturation density after a long time and A is the rate per unit volume of s-$\bar{s}$ pair production. The number of strange quarks will increase until there is saturation in phase space. This saturation will occur at time τ called the relaxation time ($\tau = \rho_s^\infty/A$). An estimate for the equilibration time is about 2-3 fm/c. Since this time is approximately equal to the expected lifetime of the QGP, we can conclude that strangeness production reaches equilibrium.

Within the enhancement framework there are two cases to be considered: low chemical potentials of up and down quarks, and high chemical potentials of the same quarks. In the first case, the densities of u, d and s quarks and their respectives antiquarks are nearly equal. Thus the probability for antihyperon (baryons with antistrangeness) formation is high. Therefore, antihyperon enhancement would be a QGP signature. The second case is when the chemical potentials of the up and down quarks are nonzero while the chemical potential of strange quarks remain constant. This is the most probable scenario at RHIC. In this case, the densities of u and d are larger than those of s and $\bar{s}$, while the densities of s and $\bar{s}$ are larger than those of $\bar{u}$ and $\bar{d}$. Then we are more likely to observe the formation of kaons enhanced in QGP.

The abundance of strange quarks will possibly help in the formation of hypermatter. Hypermatter consists of clusters with more than 3 quarks, i.e. a 6-quark system. Hypermatter formed exclusively of up and down quarks can't exist due to their large fermi energy. Nevertheless, hypermatter with strange quarks, called strangelets, may be stable. The two simplest examples of strangelets are the H-dibaryon (2u2d2s) and the strange quark-α (6u6d6s). In spite of being as massive as normal nuclei, strangelets can be distinguished in experiments by their very low or negative charge to mass ratio. However, strangelets are not the only particles with this property. Metastable Exotic Multihyperon Objects, or MEMOs, also have a very low or negative charge to mass ratio. MEMOs consist of multiple hyperons bound together. Finding hypermatter does not necessarily means that QGP was formed, but it would be another signature.

1.6.3 Chiral Symmetry Restoration

The helicity of a particle is defined as the scalar product of its spin with its momentum. A particle is said to be "left handed" if its spin and momentum are in opposite directions. If they are in the same direction, then the particle is called "right handed". Mathematically, the QCD lagrangian assumes massless quarks, which can be factorized into left handed and right handed terms, is symmetric with respect helicity. This is called chiral symmetry. Since a quark's helicity is not changed by its interactions with gluons, one might argue that it's "left-handedness" or "right-handedness" is a conseved quantity. This fact will give rise to a couple of new quantum numbers B_L and B_R. However for a massive particle we can change its helicity by boosting to a reference frame where the particle's momentum direction is reversed. For massless particles, helicity is a conserved quantity because they travel at the speed of light. Therefore massive quarks are better described as a superposition of helicity eigenstates with their masses playing the role of being the parameter between left and right transitions. Now only the sum $B = B_L + B_R$ is a good quantum number. Chiral symmetry would only occur if the quarks are massless, but since they are not we have broken chiral symmetry.

The concept of chiral symmetry helps explain why the effective mass of a quark depends upon the distance it is probed. At short distances, or the deconfinement region, the quark masses are just a few MeV. On the other hand, at large distances, the quarks are confined within hadrons and their masses are a few hundred MeV. This increment in their masses is caused by interactions among themselves and with the vacuum. Consider a quark creation and annihilation operator ψ and $\bar{\psi}$ respectively. A chiral symmetry breaking vacuum is given by:

$$< \bar{\psi}\psi >=< 0|\bar{\psi}_L\psi_R + \bar{\psi}_R\psi_L|0 >\approx (250MeV)^3 \tag{39}$$

This non-vanishing value indicates that the vacuum is not really "empty", bur rather contains a sea of quark-antiquark pairs. Physically, this value can be identified with the number of quark-antiquark pairs per unit volume in the QCD vacuum. Now consider a left-handed quark traveling through this vacuum which is destroyed by ψ_L. This would leave a $\bar{\psi}_R$ that would create a right-handed quark. So in effect it would be as if the original quark changed helicity like a massive particle. The rate of change in helicity is proportional to $< \bar{\psi}\psi >$ and that is how we can measure the value of $(250MeV)^3$. This dynamically generated mass is called the constituent mass and it's the one we observed in hadrons. If QGP is formed, we expect chiral symmetry to be restored. That is, we expect to see the quark masses approach zero. This is because the quarks will no longer be confined within hadrons and therefore we would be able to see their intrinsic or bare mass. Within the phenomelogical bag model described in section 1.3, chiral symmetry breaking is explained as follows. When a quark reaches the surface of the bag in which it's confined, it must change its direction because of confinement but not its angular momentum (which is conserved). This represents a change of helicity. Since as mentioned before, gluon exchanges are not responsible for this helicity change, it must come from the vacuum outside the bag. The quark-antiquark pairs of the QCD vacuum exchange helicity with those quarks inside the bag. Another thing we also expect to see if QGP is formed is the formation of Disoriented Chiral Condensates (DCC) that would decay into pions. DCC are coherent excitations of the pion field corresponding to a local misalignment of the chiral order parameter $< \bar{\psi}\psi >$. DCC can be detected when they decay into neutral and charged pions, because they do it in a ratio different from one third.

1.6.4 Other Probes

There are other probes besides those mentioned above. For example, the distribution of global parameters of the events, such as multiplicity and momentum spectra of the emitted particles, is another suggested probe for QGP formation. By studying these characteristics, we can infer the initial state. Sudden changes in these parameters with varying energy or mass number are indicators of a phase transition. Also, other probes are photons and dileptons. They are penetrating probes of hot and dense matter because they are produced in the early stage of the process and they are not affected by hadronization. They interact only electromagnetically, thus they pass through quark matter without interacting. However, we must be careful with photons and leptons because there are other sources that may produce them besides the hot quark matter. For instance, pions can decay to produce thermal photons. In the case of dileptons, they can also be produced by $\pi^+\pi^-$ annihilation in a hadron gas and also in the decay of low mass vector mesons such as ρ. Single leptons are not considered because weak decays of hadrons produce a strong background. As a consequence, understanding the background of photons and dileptons is very important when studying them as QGP signals. Because leptons and photons are the least sensitive to the expansion phase, they can act as thermometers, not to the final temperature, but to the temperature in the initial phase of QGP formation where their temperature-dependent production is highest. It has been estimated that:

$$EdN/d^3p \approx exp(-p_T/T_{eff}) \tag{40}$$

where T_{eff} is a measure of the final temperature of the fireball. When the collision energy is increased, then $T_{eff} \approx T_{max} = T_c$, the critical temperature for the phase transition.

Another suggested QGP signature related to the abundance of strange quark-antiquark pairs is the enhancement of the ϕ meson, which is suppresed in the hadronic gas by the OZI rule [3]. This probe is useful because the information that the ϕ carry about the inital conditions of the fireball is not lost because they have a small rescattering cross-section with non-strange hadrons. Other signatures suggested due to the rich strange antiquark environment in QGP is the enhancement of multistrange baryons such as the $\Omega^+(\bar{s}\bar{s}\bar{s})$, the anticascades $\Xi^+(\bar{d}\bar{s}\bar{s})$, and antihyperons.

1.7 Gluon Saturation

The second goal of this dissertation is to study the phenomenon of gluon saturation in the early conditions after the collisions[29-43]. When the Lorentz contracted nuclei approach each other at ultrarelativistic speeds, they appear as an infinitesimally thin two-dimensional sheet. Therefore all partons in each nuclei can "see" all other partons in the other nuclei. The density of partons per unit area is given by:

$$\rho = \frac{1}{\pi R^2}\frac{dN}{dy} \tag{41}$$

where N is the number of partons and ρ will increase as the partons have less volume to populate. Gluons will begin to overlap in the tranverse direction too, which leads them to populate higher states in p_t and to recombine until the density of partons per unit phase space is saturated. This saturation follows from the fact that if the phase space density becomes too large, gluons will repel each other because of Pauli's principle and eventually it will be energetically unfavorable to increase the density. This means that there must be a saturation scale. Saturated gluons form a Bose condensate called Color Glass Condensate (CGC) [44-46]. This happens at scale of order $1/\alpha_s$. The momentum scale associated with the saturation is called Q_s and is given by:

$$Q_s^2 = \frac{8\pi^2 N_c \alpha_s}{N_c^2 - 1} xG \frac{\rho_{part}}{2} \tag{42}$$

where N_c is the number of colors in the theory, ρ_{part} is the density of participants in the tranverse plane and xG is the gluon structure function of the nucleon. If we defined G as the number of gluons per unit x ($x \approx p_L/\sqrt{s}$):

$$G = \frac{dN_g}{dx} \tag{43}$$

then the gluon structure function xG has the general form:

$$xG = x\frac{dN_g}{dx} = \frac{dN_g}{d(lnx)} \tag{44}$$

At RHIC, $x \approx 0.02$, $xG \approx 2$ and $Q_s^2 \approx 1 - 2GeV^2$. This saturation scale is also characterized by a variable called Λ_s which is related to Λ_{QCD} by:

$$\Lambda_s^2 = \Lambda_{QCD}^2 A^{1/3}/x^{\delta} \tag{45}$$

where A is the atomic weight of the nucleus and δ is a numerical constant. For high energies and large nuclei, such as gold, we have that $\Lambda_s^2 \gg \Lambda_{QCD}^2$, the coupling constant is weak and the occupation number is large. In this regime, lattice QCD methods can be used to calculate the initial energy density as well as the gluon tranverse density per unit pseudorapidity. These quantities are expressed in terms of the coupling constant g and Λ_s. They are:

$$\epsilon = \frac{0.17}{g^2}\Lambda_s^4 \tag{46}$$

and

$$\frac{1}{\pi R^2}\frac{dN}{d\eta} = \frac{0.3}{g^2}\Lambda_s^2 \tag{47}$$

where the constant coefficients in the right side of the equations were obtained numerically. This method also allows to find a relation between the initial gluon multiplicity and the final hadron multiplicity. It is given by:

$$dN^h/d\eta = \kappa dN^g/d\eta \tag{48}$$

where κ is just a proportionality constant that can be found experimentally. Therefore, within the CGC approach, and using RHIC results we could test these predictions of gluon saturation. In the last section of this dissertation, we'll try to build a bridge between the theory presented in this section, particularly that of the saturation scale Q_s, and the observables at STAR.

2 EXPERIMENT

2.1 The Relativistic Heavy Ion Collider

Collisions for our experiment took place at the Relativistic Heavy Ion Collider (RHIC) at Brookhaven National Laboratory (BNL). RHIC is designed to accelerate gold nuclei in two opposite rings to energies up to 200 GeV per nucleon pair in the center of mass. However in the first year run (summer 2000) the energy achieved was only 130 GeV per nucleon pair. RHIC also has the capability to collide other heavy ion species as well as polarized protons. Polarized protons will be used to study the spin structure of the proton. This is interesting because previous experiments tell us that the intrinsic spins of all quarks and antiquarks only account for less than 30% of the nucleon's spin. Therefore the remaining 70% of the nucleon spin must come from the relative orbital motion of the quarks and gluons inside. Even though RHIC can deal with protons, the data analyzed in this thesis was from heavy ion collisions, so from this point on we will focus on them.

RHIC is not the first accelerator to study heavy ion collisions. As mentioned in the introduction, previous experiments in the field of relativistic heavy ion physics were perfomed during the 1980's and 1990's at the Alternating Gradient Synchrotron (AGS) at BNL, and at the Super Proton Synchrotron (SPS) at CERN. The AGS used silicon and gold beams up to energies of 5 GeV per nucleon pair. SPS used sulfur and lead beams up to energies of 17 GeV per nucleon pair. Unlike RHIC, these were fixed target experiments. The results obtained at RHIC will be compared to those obtained at those two accelerators. Also at CERN, the Large Hadron Collider (LHC) is being built and is scheduled to start taking data in 2007. The LHC will accelerate lead up to 6300 GeV per nucleon pair, starting a new generation of this type of experiments.

The process of accelerating a gold ion to 65 GeV per nucleon involves several accelerators that make up the RHIC complex. Figure 5 shows the RHIC complex. The ion beam starts its journey in the Tandem Van de Graaff. It consists of two 24 meters and 15 million volts electrostatic accelerators that can provide up to 40 different kinds of ions, including gold. Here an electric field begins accelerating the ions and send them to the Heavy Ion Transfer Line (HITL). Once the ions reach the HITL, they are carried through a vacuum using a magnetic field, traveling at 5% of the speed of light. Then the ions are provided with more energy at the Booster accelerator with electromagnetic waves. In the Booster accelerator they reach a speed of 37% that of light. From there, the ions make their way to the AGS where they reach 99.7% of the speed of light. The AGS consists of 240 magnets. The field gradient of these magnets is alternated, hence the name. Once they are travelling at this ultra-relativistic speed, they are transfer to RHIC via the AGS-To-RHIC (ATR) transfer line. Once they reach the end of the ATR transfer line, the ions are divided into 2 bunches, travelling either clockwise or counterclockwise in the so-called blue and yellow lines. RHIC itself is made up of hundreds of magnets that made up a ring of 3.8 kilometers in circumference. See figure (6) for a cross-section view of a RHIC magnet. RHIC's maximum design luminosity is $2 * 10^{26} cm^{-2} s^{-1}$, however on the first year of run, it only reached 10% of that value. Luminosity is the number of ions passing per unit area per unit time. It can be calculated by:

$$L = f \frac{n_1 n_2}{4\pi\sigma_x\sigma_y} \tag{49}$$

where n_1 and n_2 are the number of ions contained in each of the bunches colliding with frequency f, and σ_x and σ_y are the widths of the beam in the x and y directions (perpendicular to the beam axis). Luminosity is a useful quantity because the event rate R in a collider is proportional to the luminosity L times the interaction cross-section:

$$R = L\sigma_{int}. \tag{50}$$

The effect of synchrotron radiation, which has to be taken into account on electron-positron colliders, is negligible at RHIC due to the large mass of the gold ions. We can verify this statement by calculating it ourselves. The centripetal acceleration of a relativistic particle causes it to radiate energy at a rate given by [47]:

$$P = \frac{1}{4\pi\epsilon_0} \frac{2}{3} \frac{q^2 a_c^2}{c^3} \gamma^4 \tag{51}$$

where P is the power, q is the charge, and a_c is the centripetal acceleration. We also know that the time it takes the ion to go around one turn at the accelerator is:

$$t = 2\pi R/v \tag{52}$$

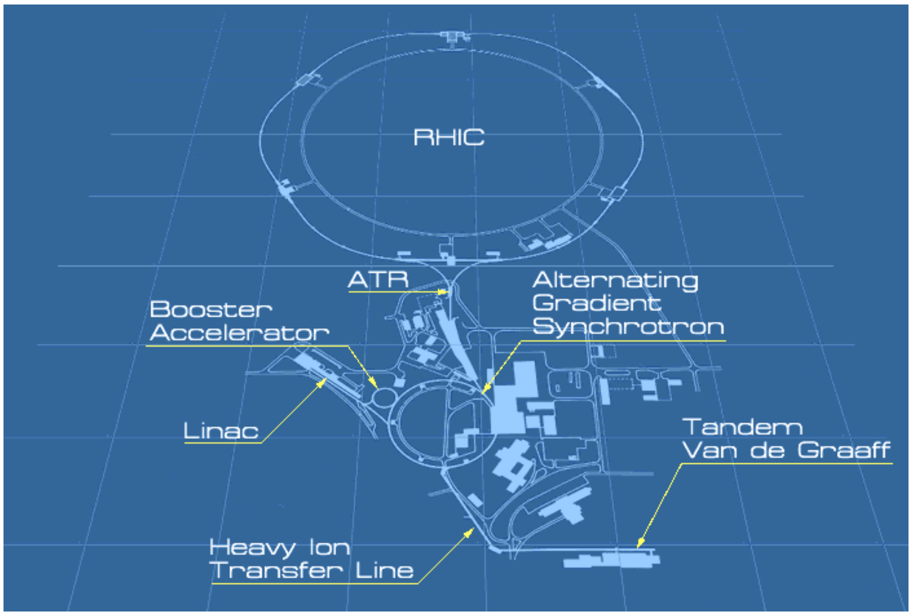

Figure 5: RHIC complex. The journey of the gold ions start at the Tandem Van de Graaff and ends at the RHIC ring. See text for details on each of the accelerators.

where v is the speed of the ion, and R is the accelerator radius. Therefore the energy lost by the ion in one turn is:

$$\delta E = P \cdot t = \frac{1}{3\epsilon_0} \frac{q^2}{Rc^8} \frac{E^4}{m^4} \tag{53}$$

where we have replaced a_c by its definition:

$$a_c = v^2/R \tag{54}$$

and γ by using the Einstein's energy-mass relation:

$$E = \gamma mc^2 \tag{55}$$

and letting $v \approx c$. We can now estimate the energy lost per turn for a gold ion to be around 1.4 eV at RHIC. Since $\delta E/E \approx 10^{-13}$, it is indeed negligible.

RHIC has six intersection points where the beams can collide. At four of those points there are experiments being performed. The names of the experiments are PHOBOS, BRAHAM, PHENIX, and STAR. PHOBOS, named after a Mars satellite, is a small experiment. It looks for rare but interesting events among a large number of collisions. For each collision, PHOBOS gives a global picture of the consequences of the collision and detailed information about a small subset of the nuclear fragments ejected from the fireball. BRAHMS, or Broad Range Hadron Magnetic Spectrometers, is also a small experiment. It measures particles at specific angles. It also has the capability of measuring inclusive momentum spectra of identified charged hadrons over a wide range in rapidity and tranverse momentum. PHENIX, or Pioneering High Energy Nuclear Interaction Experiment, is one of the large experiments. It looks for leptons, photons, and hadrons. It will also be sensitive to small cross section processes. STAR, or Solenoidal Tracker At RHIC, is the other large experiment. STAR is our detector and it will be described in a little more detail in the rest of this chapter.

2.2 The STAR Detector

The Solenoidal Tracker At RHIC (STAR) is searching for some of the QGP signatures described in chapter one. Its emphasis is the correlation of many observables on an event by event basis. Some of the observables that STAR measures are charged hadrons, neutral hadrons, spectra, collision geometry, and strangeness production. STAR has complete azimuthal coverage over the central rapidity region. This is nec-

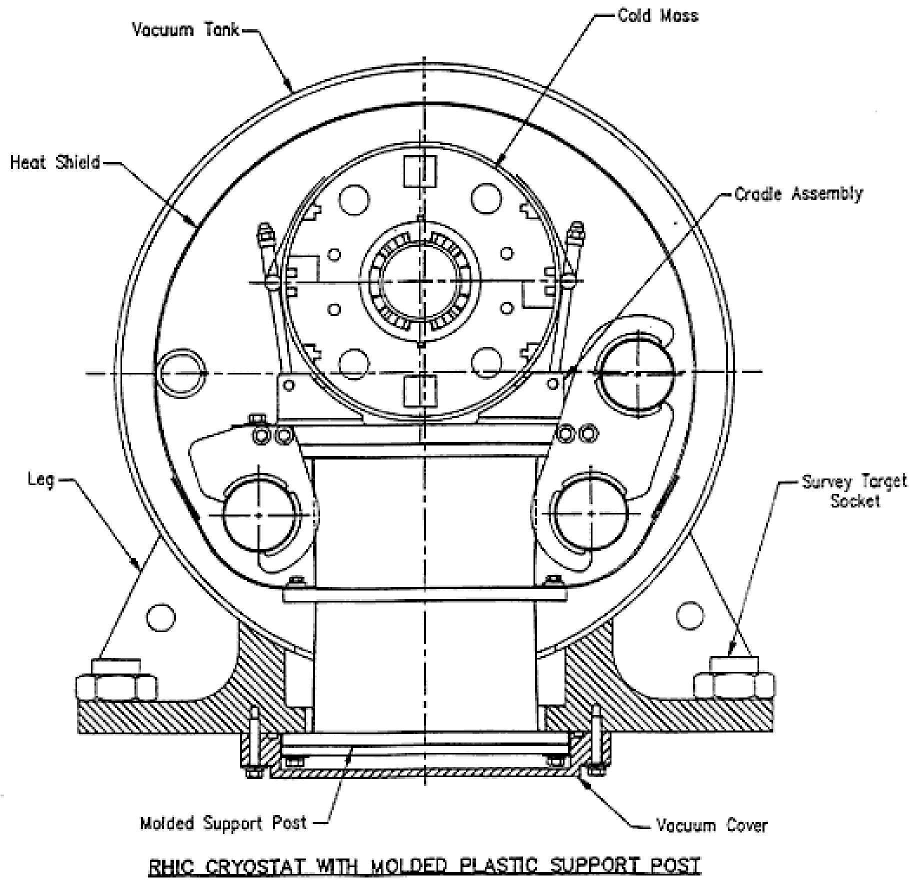

Figure 6: Cross sectional view of a RHIC magnet. The pipe in the middle is where the heavy ions travel. That pipe is only a few centimeters across.

essary to measure the observables at momenta where the particles yields are maximal. The central rapidity region also offers the best conditions for forming QGP [10]. Besides the event by event measurements, STAR also measures hadronic cascades of hard-scattered partons that are used as a penetrating probe of QGP. STAR will also be able to study peripheral collisions, where the nuclei physically miss each other, but interact via longer ranged forces.

Momentum measurements are made at midrapidity over a range of $|\eta| < 2$. Particle identification is performed within $|\eta| < 1$. STAR is located within a 0.25 Tesla solenoidal magnet. STAR consists of several detectors, among them the Time Projection Chamber (TPC) which is the main tracking chamber. It covers the pseudo-rapiditiy range of $-0.88 < \eta < 0.88$. The TPC provides particle identification via dE/dx. In addition to the TPC, there is the Forward TPC (FTPC), which extends the coverage in rapidity. There's also a Silicon Vertex Tracker (SVT) which together with the TPC and the FTPC are used in reconstructing secondary vertices of neutral particles decaying to charged particles away from the primary vertex. There's also an electromagnetic calorimeter (EMC) which provides complete coverage for electromagnetic physics. These are the so-called "slow detectors" because of their relative long readout times. A brief description of each of these detectors is given in sections 2.3 to 2.6. The triggers ("fast detectors") are described in section 2.7. A diagram showing the relative position of each component within STAR is found below (figure 7) as well as a side view of the components (figure 8).

STAR is designed to measure both soft and hard physics observables. Soft physics is in the range of $0.1GeV < p_t < 1.5GeV$. The physics above 1.5 GeV is called hard physics. A few of the obsevables in each of these regions are described below.

Soft Physics:

• Detection of charged particles to provide high statistics.

• 2π azimuthal coverage.

• High kaon detection efficiency.

• Momentum resolution $\triangle p/p < 0.02$.

• Determination of the primary vertex for high momentum resolution.

• Determination of secondary vertices for detecting strange particle decays.

Hard Physics:

• Large acceptance to maximize rates and minimize edge effects in jet reconstruction.

• Determination of the primary vertex to achieve a momentum resolution $\triangle p/p < 0.05$ for high p_t particle spectra and jets.

• Linear response of electromagnetic calorimeter for energy measurements.

2.3 Magnet

The magnet is a solenoid with a uniform magnetic field along the beam direction. Its maximum strength is 0.5 T. However, on the first year run it was 0.25 T. The magnet has a length of 6.9m. The radius of the iron return yoke is 2.87m. The weight of this magnet is 540 tons. This magnet was designed in such a way that

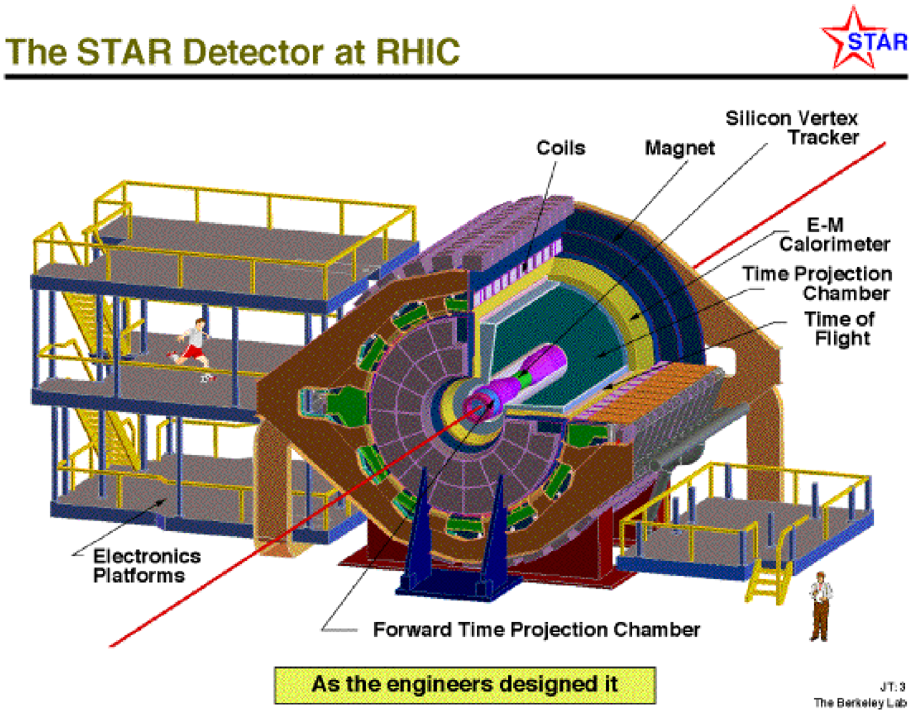

Figure 7: Front view of the STAR detector showing several components as well as its relative size compared to a person.

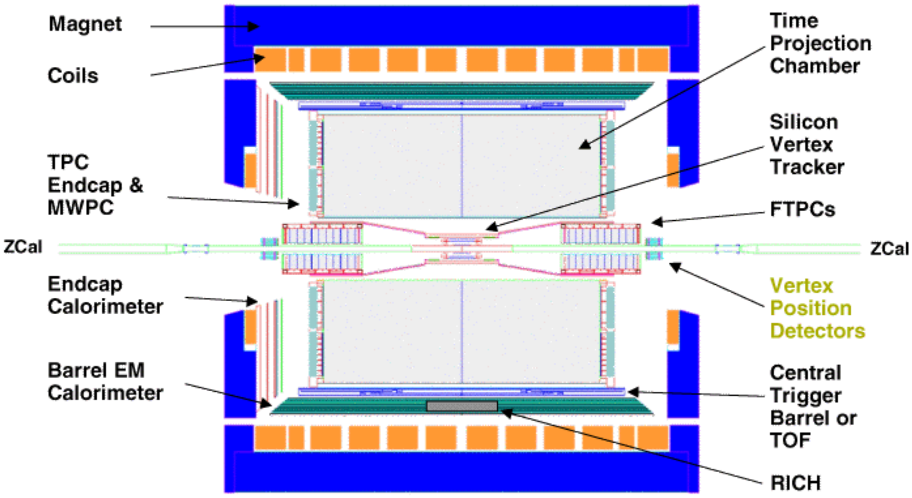

Figure 8: Side view of the STAR detector showing most of the subsystems.

it provides high tracking accuracy and azimuthal symmetry. The magnetic field is very uniform, with non-uniformities approximately 1 part in 1000. This uniformity is partly achieved by superconducting and conventional correction coils.

2.4 Time Projection Chamber

For our purposes the TPC is the main component of the STAR detector since it is the one we used for particle identification. Therefore we would like to explain it in a little more detail. It is a drift chamber with a multi-wire proportional chamber at both ends for readout. Its external electric field is produced by the outer field cage, the inner field cage and the high voltage central membrane. Figure (9) shows the relative position of each one of these components in the TPC. Both the outer and inner field cages are also used to define the active gas volume. They help prevent contamination from outside air. Figures (10) and (11) show the design of both field cages. The central membrane is held a high voltage. This membrane divides the TPC into twp longitudinal drift regions called TPC east and TPC west because of their location in the STAR experimental hall. At both ends of the TPC there are a total of 144,000 pads which give x-y coordinate information and 512 time buckets which provide z coordinate information for each hit. These pads are divided into 24 sectors. Within each sector, the pads are arranged in 45 rows. Rows 1 through 13 are called the “inner” sector, while rows 14 through 45 are known as the “outer” sector. In the inner sector the pads are 2.85 mm by 11.5 mm with a separation of 3.35 mm. In the outer sector they are 6.2 mm by 19.5 mm with a separation of 6.7 mm between pads.

Figure (12) shows the pad distribution in a particular sector. Charged particles can be detected in drift chambers because they ionize the gas along their flight path. The energy for the gas ionization is taken away from the kinetic energy of the particles. The gas in the TPC is a mixture of argon (90%) and methane (10%). This mixture is known as P10. This mixture was chosen taking into account issues such as gas purity, multiple scattering, drift velocity, cost, and safety. The drift velocity is proportional to the externally applied electric field, but it is not linear and it depends on the gas composition (see figure 13). To obtain better track reconstruction it is better to select an electric field near the peak in the drift velocity curve. That way, the drift velocity is saturated and therefore less sensitive to environmental changes. One very interesting fact about the STAR TPC is that with a length of 4.2m and a outer radius of 2m, it is the largest in the world.

Figure (14) shows the TPC software chain (simulation and analysis) which is used in the event reconstruction. The objective of the software chain is to take the raw data from an event and obtain physical quantities which are useful to the analysis. In figure (14) the event generator (Hijing) is a Monte Carlo generator for particle production in high energy nuclear collisions. In the same figure, GSTAR refers to the framework used to run simulations using GEANT. The GEANT program simulates the passage of particles through matter. The distortion simultations package takes into account the effect of the electric field in the TPC, for zero magnetic field, cosmic rays, and laser tests. The fast simulator package is designed to simulate the TPC response to the passage of charged particles throught the TPC volume. The TTE (TPC Tracking

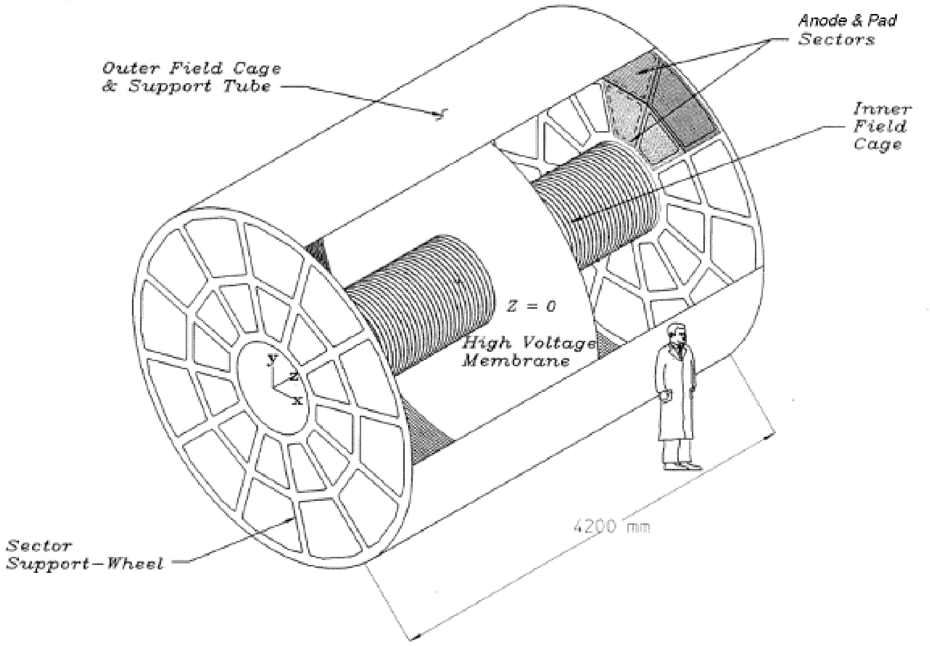

Figure 9: Diagram of the Time Projection Chamber showing the locations of the central membrane and the field cages.

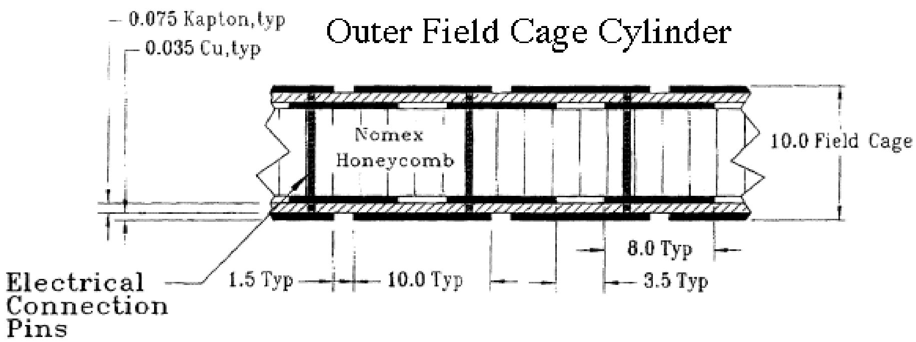

Figure 10: Outer Field Cage: It is designed to allow particles pass through it but it must also be gas tight.

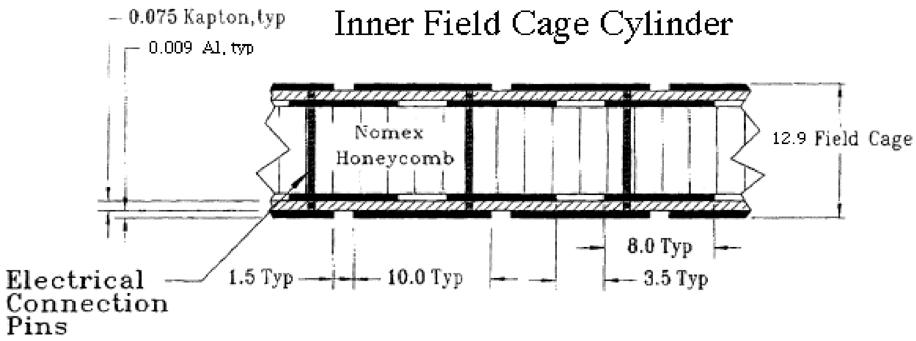

Figure 11: Inner Field Cage: Its properties are similar to those of the outer field cage.

Evaluation package) is required to estimate quality of the track reconstruction. The TPT (TPC Tracking package) consists of 2 modules that use reconstructed TPC hits as input. The MiniDAQ is a data acquisition system that can deliver data from one TPC sector to tape or online processes. However, MiniDAQ does not have the same capabilities as DAQ. Using all these packages there are 3 ways to simulate or analyze the data: first, the fast path, where the output from GSTAR is processed by the fast simulator and input to the track finding. Second, the slow path where the output is processed by the slow simulator and input into the hit finder and then the tracking (TPT). Third, the analysis of the test data where the output from the MiniDAQ is corrected and then hits are reconstructed and the events are tracked.

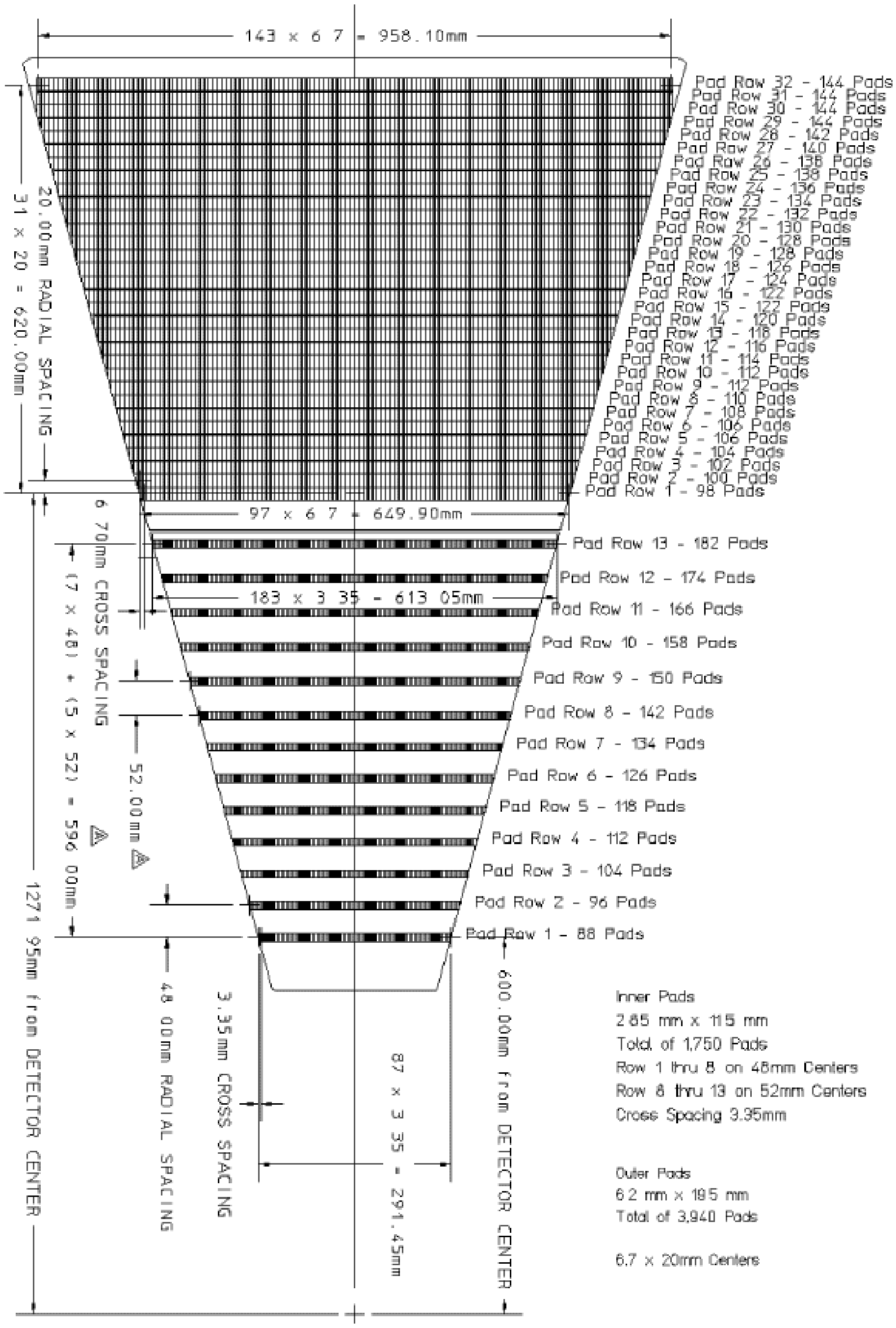

Figure 12: Pads distribution in a TPC sector. The number of pads on each row can be seen to the right.

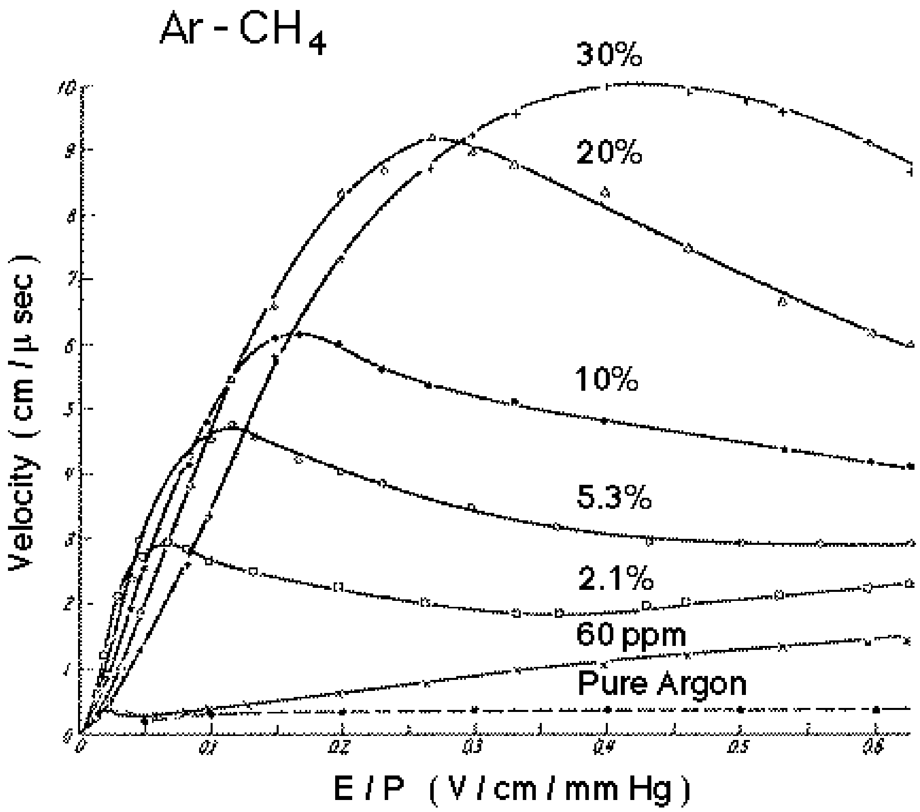

Figure 13: Drift velocity as a function of the electric field for several mixtures of argon and methane. The mixture used at STAR (P10) was chosen taking into account several issues explained on the text.

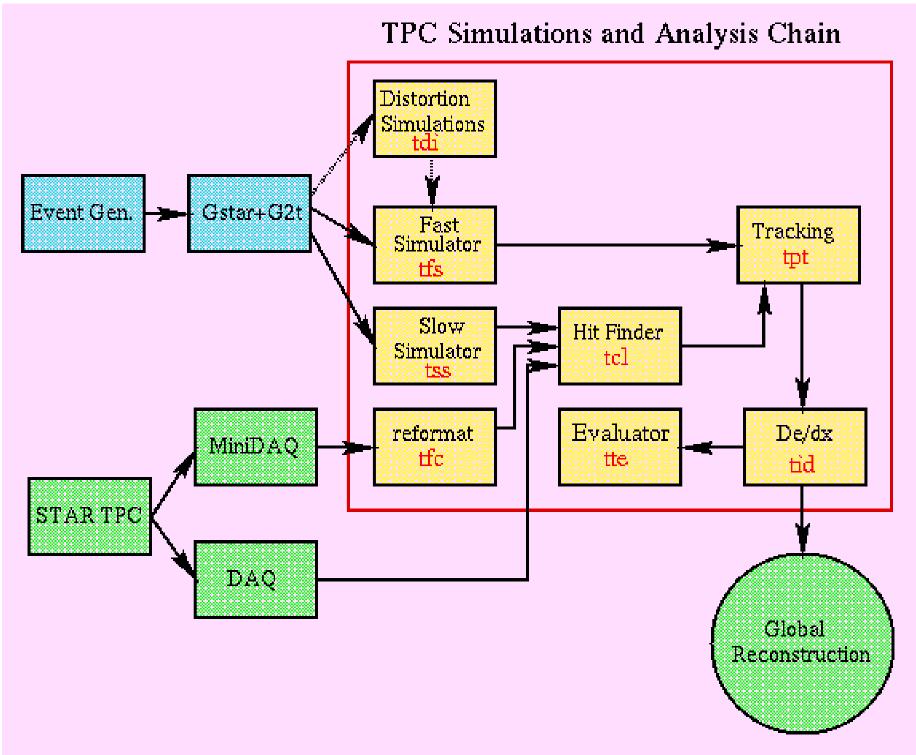

Figure 14: TPC software chain used for both simulations and data analysis. The description of each step is found on the text.

2.5 Silicon Vertex Tracker

The SVT helps the TPC locate the position of the primary vertex. It also improves the momentum resolution of the detector by enhancing the capabilities of the TPC to include low momenta tracks. Particle identification through the measurement of dE/dx with the SVT is also possible. The SVT helps in the detection of charmed particle production as well. It consists of 162 silicon drift detectors (SDD) grouped into ladders. Theses ladders are located in 3 concentric barrels of 8, 12, and 16 ladders with radii of 5, 8 and 11 cm respectively. Each barrel is 42 cm in length. Each wafer SDD has an area of 6cm x 6cm and a thickness of 280 microns. The wafers are split in 2 and are read out at both ends. Each wafer has a total of 480 anodes read out and the signal from each one is sampled and stored. Figure (15) is a cross-sectional diagram of the SVT.

2.6 Electromagnetic Calorimeter

The purpose of the EMC is to measure the total and local tranverse energy deposition in the collisions. Such measurements are necessary to determine the degree of nuclear stopping power which occurs. With the EMC we can also obtain the temperature and energy density characterizing the reaction. This is achieved by analyzing the total tranverse energy at mid-rapidity. It can also be used to search for fluctuations in particle production. Event by event correlation of distributions facilitates the identification of rare events. Because the EMC can detect neutral electromagnetic

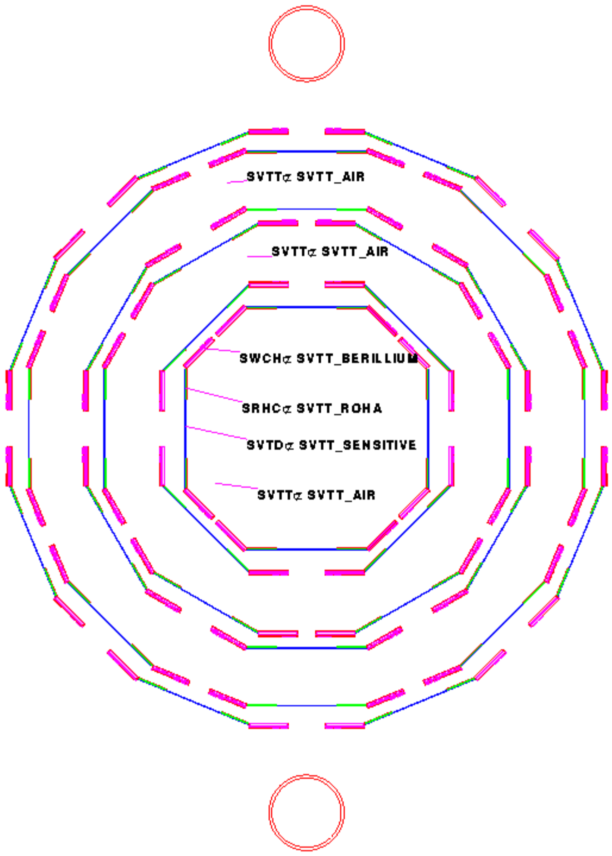

Figure 15: SVT: view perpendicular to the beam axis.

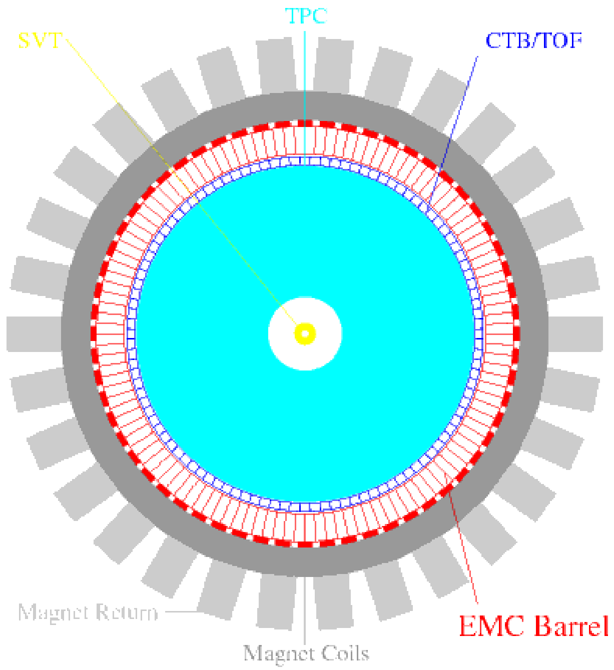

Figure 16: Front view of the EMC showing its relative position with respect other STAR components.

energy, it performs several functions in the study of these phenomena. It also can differentiate between electromagnetic and hadronic energy. The EMC consists of a barrel which is a lead scintillator sampling calorimeter. The EMC barrel is arranged into 120 modules. It has a length of 6.87 m and an inner radius of 2.53 m. It weighs about 150 tons. Its azimuthal coverage angle is 2π and its pseudorapidity range is $|\eta| < 1.05$. Figures (16) and (17) show two views of the EMC where we can see its relative position with respect other STAR components.

2.7 Triggers

The trigger system at STAR is design to look at every event and decide whether or not to accept it. Figure (18) is a schematic diagram of all the trigger detectors.

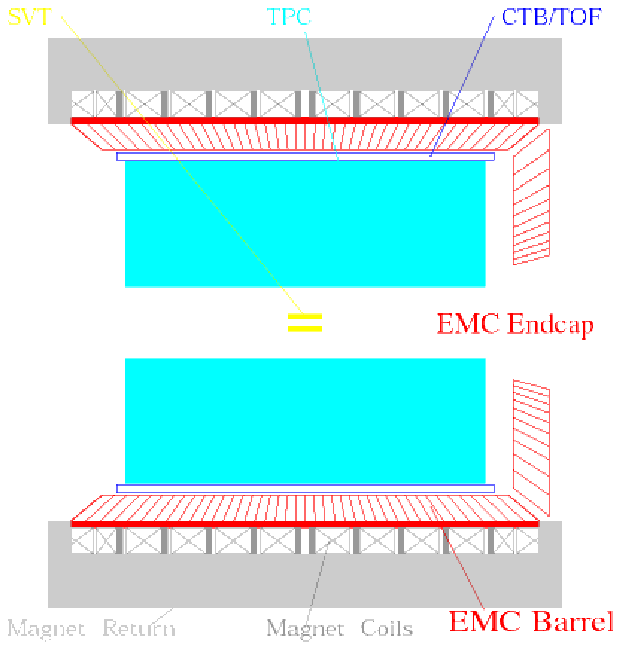

Figure 17: Side view of the EMC where the location of the endcap can be seen.

These detectors are called the "fast" detectors, as opposed to the "slow" detectors described above. STAR used a central trigger barrel (CTB) to trigger on collision centrality. It consists of 240 scintillators slats surrounding the TPC. It measures charged multiplicity in range of $|\eta| < 1$ and complete azimuthal coverage (see figure 19). In addition to the CTB, there are two zero-degree calorimeters (ZDC) located downstream of the dipole magnets at 18 meters of the interaction region. Their dimensions tranverse to the beam is 10 cm x 10 cm. They measure the energy in neutral particles within a 2 mrad cone about the beam direction. This capability makes the ZDC useful to measure the collision centrality since the energy it measures is correlated to the number of spectator neutrons. The ZDC is made out of layers of lead and scintillator fibers. Each one consists of 3 modules, each of which is readout with a separate photomultiplier tube (see figure 20). Figure (21) shows the correlation

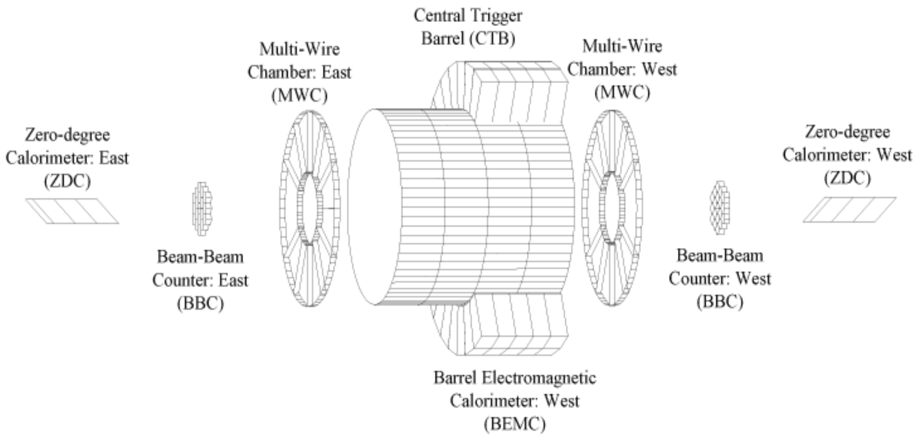

Figure 18: Relative position of the trigger detectors at STAR. The CTB and the ZDC were the most important for our analysis.

between the CTB and the ZDC. When the impact parameter is large, the multiplicity in the central region is small, therefore the count on the CTB is low. Also, the number of spectator neutrons is small, so the count on the ZDC is also low. When the impact parameter decreases, the multiplicity in the central region increases and the count on the CTB will increase. The effect on the ZDC is that of increase on multiplicity until a saturation of spectator neutrons is reached and then decreases. Therefore the largest multiplicity occurs at high CTB and low ZDC. This will correspond to most central collisions. We can then perform cuts on the CTB and the ZDC to obtain collision centrality. Details of the centrality cuts used for data analysis are given on section 3.2.

The trigger system consists of 4 levels of analysis. They are called Level 0, Level 1, Level 2 and Level 3. But of those, only 3 levels use the fast trigger detectors. Level 0 recieves data from the detectors and accepts events. This layer looks at every RHIC crossing and decides whether to accept the event or not. The time allowed between a

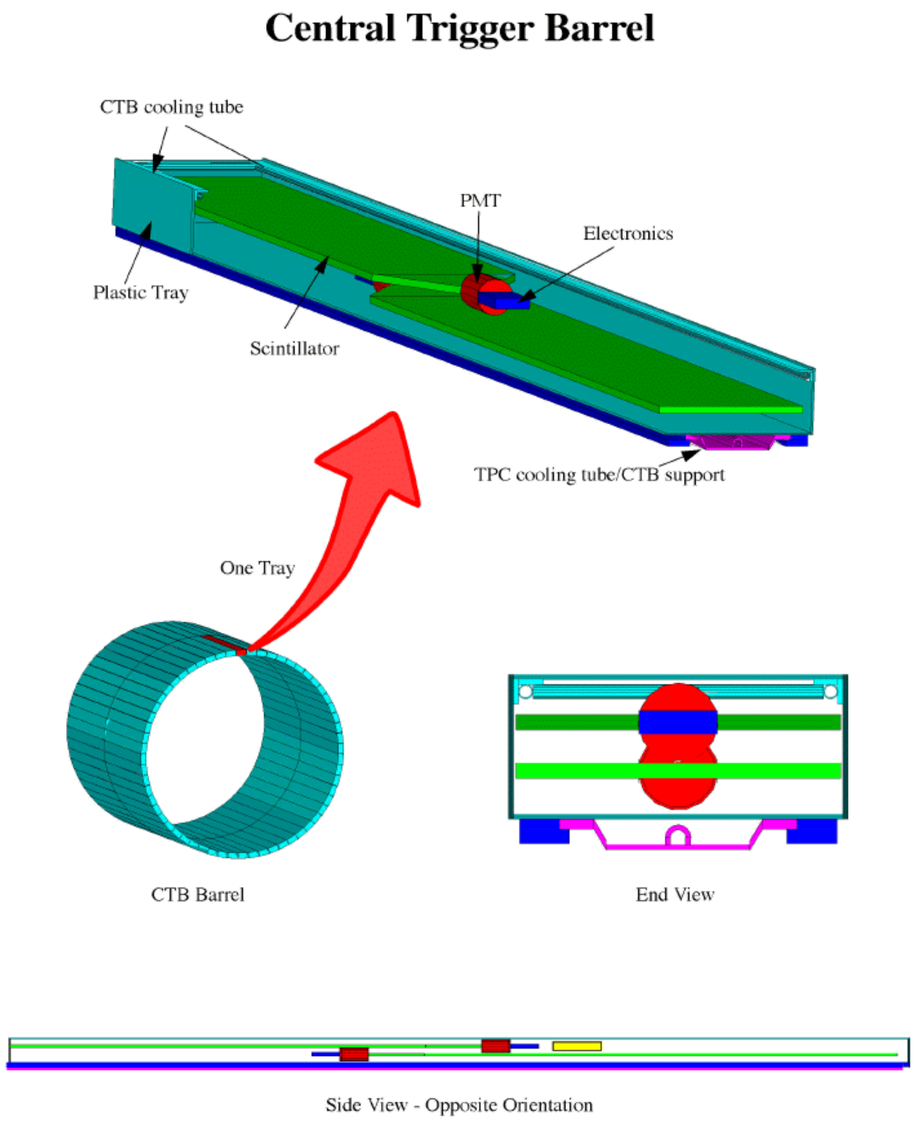

Figure 19: View of the components of one of the trays that make up the CTB barrel.

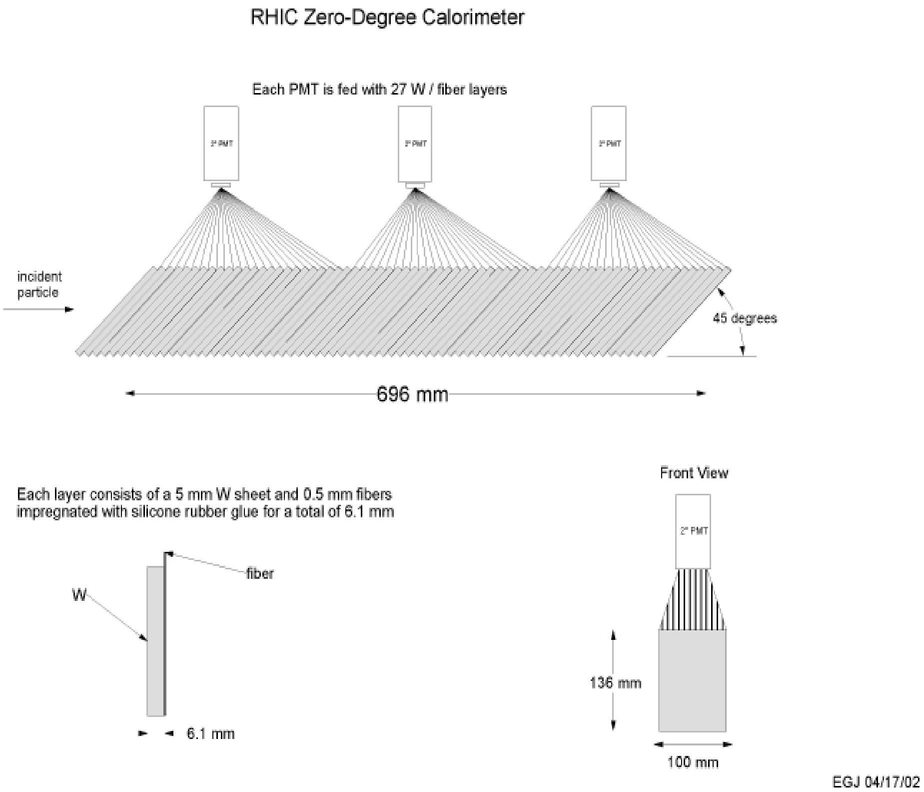

Figure 20: Diagram of the composition of the ZDC.

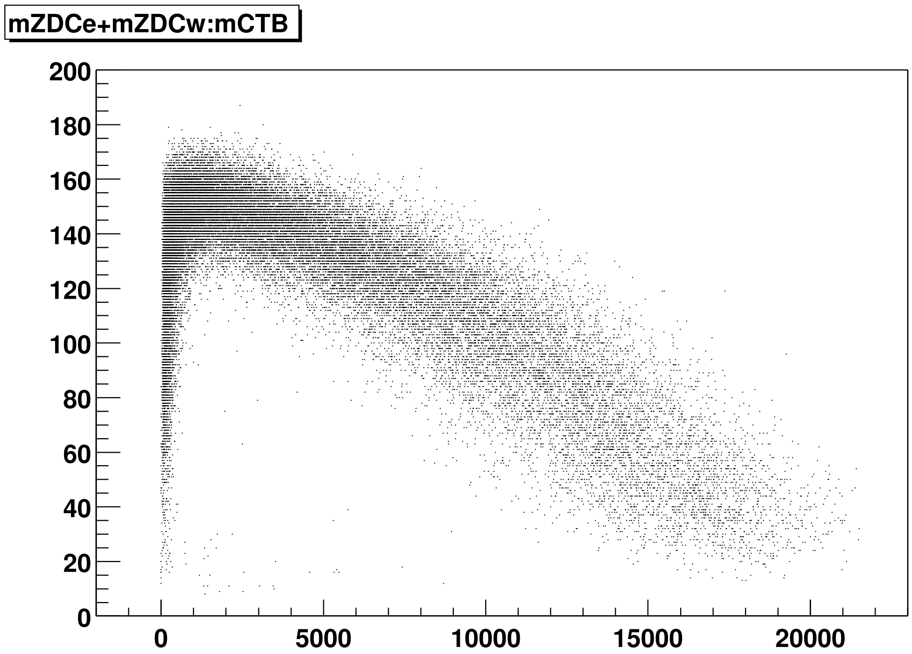

Figure 21: Correlation between the ZDC and the CTB used to trigger centrality. Central collisions are located at the lower right corner. See text for details.

RHIC crossing and the Level 0 decision is 1.5 microseconds. The Level 0 data consists of multiplicity count, energy deposits and vertex location. Level 0 is made up of 2 pieces: a data storage and manipulation board (DSM board) and a Trigger Control Unit (TCU). The DSM boards recieve and store data from the trigger detectors. The TCU accepts data from the DSM board and compare it with some parameters to decide if it should be accepted. If the event is accepted, then it is passed to Level 1. In addition to the input from Level 0, all the ZDC data is available in Level 1. Level 1 has 100 microseconds to either reject the data or pass it to Level 2. Level 2 is the final pre-data acquisition layer of processing. At this level, all of the fast detectors data is available. This include all of the raw data. Level 2 has 5 miliseconds to abort the event or pass it to data acquisition. The whole procedure can be better appreciated

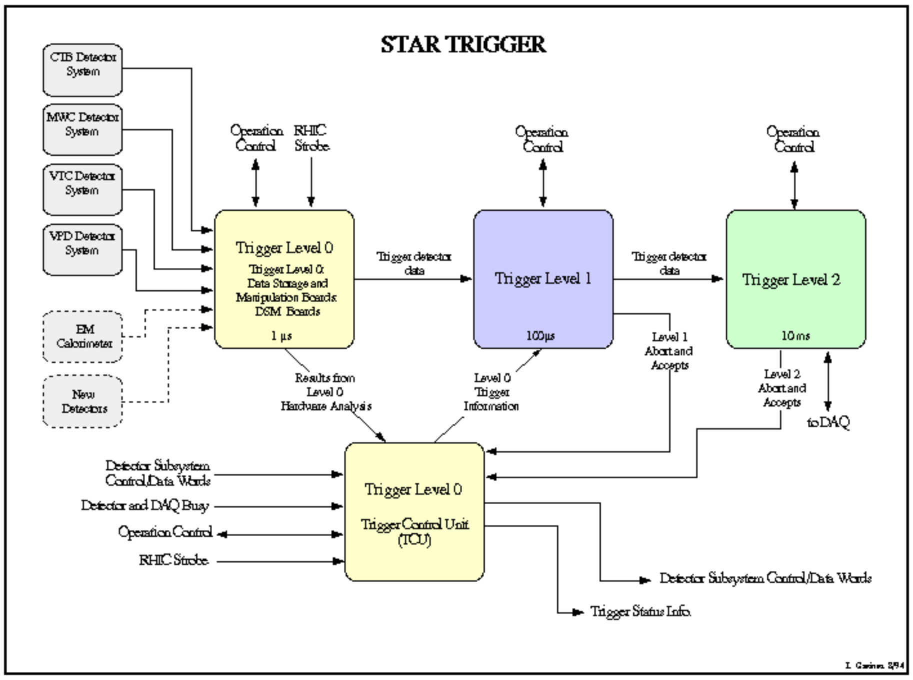

Figure 22: Trigger levels. See text for details on each level.

in figure (22), where we can see not only the relationship among different levels, but also the time it takes each level to make a decision.

2.8 Data Taking

The data analyzed in this thesis was taken during the first year of operations of RHIC, commonly known as year-1 or run-1. This run occured between the months of June and September of 2000. RHIC was operated 24 hours a day, 7 days a week. In order to take data continously, the day was divided into three 8-hour shifts. During each shift the experiment was in the hands of a team of especially trained STAR collaborators. The shift leader was the person in charge of the team and the overall supervision of the experiment. He ensured that a written log was maintained during the shift where details were kept as well as a summary of each shift. He also acted as liaison with the Main Control Room. There was also a detector operator in charge of the STAR detector. He had the responsibility to start all systems and help the shift leader decide when to start a run. There was also a Run-Time Operator which would start and stop a run, and also select the trigger. Another person was in charge of the online production quality assurance (QA). The offline production QA person had the job to monitor the validity of data, calibrations and event reconstruction from the full experiment. He or she would fill in a web based report form at the end of the shift giving detailed comments. This person would also report any problems observed in the production to the production staff. The shift crew member was in charge of checking the TPC gas room once per shift, as well as several other parameters from the experiment (temperature, dew point, etc.) every hour. He or she also had to check that all alarms were working properly. In addition to these persons, there were subsystems experts that even though were not physically at the experiment site, were always on call. It was the responsibility of the shift leader to call the experts when needed. This team of people had the authority to shut down the detector in case of any problem. The most common problem used to be power shortages due to thunderstorms. The particular training needed to perform any of these jobs, varies from one to the other, but they all could be taken either at BNL or through the web.

In addition to the group of people described above, there were two other positions that even thought were not directly involved in data taking, played an important role in the experiment. One of them was the Period Coordinator, the person that had the job to oversight the STAR experimental scientific program on a day-to-day basis for a period of two weeks. He also briefed the shift leader concerning the objectives of the running period. The second position was the Operations Coordinator whose responsibility was to coordinate technical effort.

2.9 STAR Organization

The STAR experiment has over 400 scientists from 33 institutions representing 8 countries. Such a large collaboration requires good organization in order to function properly. The STAR Council deals with general issues inside the collaboration. The council is formed by members representing every institution that is part of the experiment. One function of the council is to amend the bylaws of the collaboration. Another important function of the council is the election of the spokesperson and to confirm the deputy spokesperson nominations. The spokesperson represents the collaboration in scientific, technical, and managerial concerns. The deputy spokesperson provide support to the spokesperson in the management of the experiment. There is also an Advisory Board consisting of 12 members which function is to advice the spokesperson and the council on issues of major importance to the collaboration, such as scientific priorities of the experiment, beams use request, and STAR budget allocations.

Besides these managerial organization just described, there is also a "physics organization". The actual data analysis is divided among physics working groups which reflect different topics or aspects of physics. Each one of this physics working groups is directed by one or two co-convenors. These physics working groups are: spectra, event-by-event, HBT, high-p_t, strangeness, spin, and peripheral collisions. The physics done on this dissertation belongs to the spectra working group.

3 ANALYSIS

3.1 Kaons

In this chapter we describe the analysis used to obtain the charged kaon spectra and the results that are discussed on chapter 4 . The analysis consisted of several steps which can be summarized as follows:

• Identify the charged kaons and separate them from the other species of particles by using the energy loss method (dE/dx).

• Simplify dE/dx by introducing a new variable called "z".

• Fit the z distribution to gaussians to obtain the raw yield of particles.

• Correct the raw yield to take into account electron (positron) contamination, detector efficiencies, and energy loss.

Once the corrected yields were obtained we were able to compare it with previous experiments and determine if there was or not enhancement in strangeness production (see chapter 4). The rest of this chapter will go into details on how all these steps were done.

The first couple of questions that come to mind when analyzing the charged kaon production are: what are kaons? and why are we studying them as opposed to other species of particles? Kaons are mesons and have a quark content of $u\bar{s}$ for the K^+

and $\bar{u}s$ for the K^-. Because they contain strange quarks, they are termed strange particles. They have a mass of 494 MeV/c^2 and a mean life of $1.24 * 10^{-8}$ seconds. This mass is the lowest mass among all strange particles, and therefore they carry a large fraction of the strangeness produced in heavy ion collisions. Their mass is between those of pions and protons (antiprotons), therefore their production rate will fall between that of those two species. However, because the strange quarks are not as easily produced as the up or down quarks, the kaons production rate tends to be suppresed in the purely hadronic gas scenario (see section 1.6.2). At low energies they are produced either by pair production, with processes with the following form [48]:

- N+N $\rightarrow$ N+N+K^+ +K^-
- $\pi + \pi \rightarrow K^+$ +K^-
- $N + N^* \rightarrow$ N+N+K^+ +K^-

. Note that in pair production, K^+ and K^- are produced in equal number. In addition, due to the u quark in the colliding nuclei (net baryon density effect), K^+ are also created in associated production:

- p+N $\rightarrow$ N+K^+ +Y .
- N+Δ^+ $\rightarrow$ N+K^+ +Y .
- π+N $\rightarrow$ K^+ +Y .
- $\pi + \Delta \rightarrow K^+$ +Y .

where Y is a hyperon (Λ or Σ). Therefore at the AGS and the SPS energies, we see a larger number of K^+ than K^-. At RHIC higher energies, where the net baryon density is lower, we would expect that the contribution of the associated production will be reduced with respect the pair production contribution. This means that the production rate of K^+ should approach that of K^-. This phenomenon will be further discussed on the results chapter.

3.2 Data Sample and Cuts

The data we analyzed were acquired during RHIC's first year run, in the summer of 2000. The center of mass energy achieved at this run was 130 GeV per nucleon pair. We studied the data at mid-rapidity, which is defined as $|y| < 0.1$. The mid-rapidity region is of particular interest to us for reasons described on chapter one and on reference [10]. We restricted the primary vertex to be located within 30 cm from the center of the TPC along the collision axis (z-axis). This cut on the z vertex was done due to some irregularities in the TPC material at around 35 cm, which are explained on detail on section 3.7. Only primary tracks were used, defined as those whose distance of closest approach (DCA) was within 3 cm of the primary vertex. We performed a check that our Monte Carlo matched the data DCA distribution to make sure this cut would be taken into account in our efficiency (see figure 23). Each track was required to have at least 25 hits on the TPC. Since each sector on the TPC has 45 rows (see chapter 2) a maximum of 45 hits was possible. Just as was done with the DCA, the number of hits distribution was checked for agreement between MC and data (see figure 24). A summary of all these cuts is given below:

•$|y| < 0.1$

•$|Z_{vtx}| < 30cm$

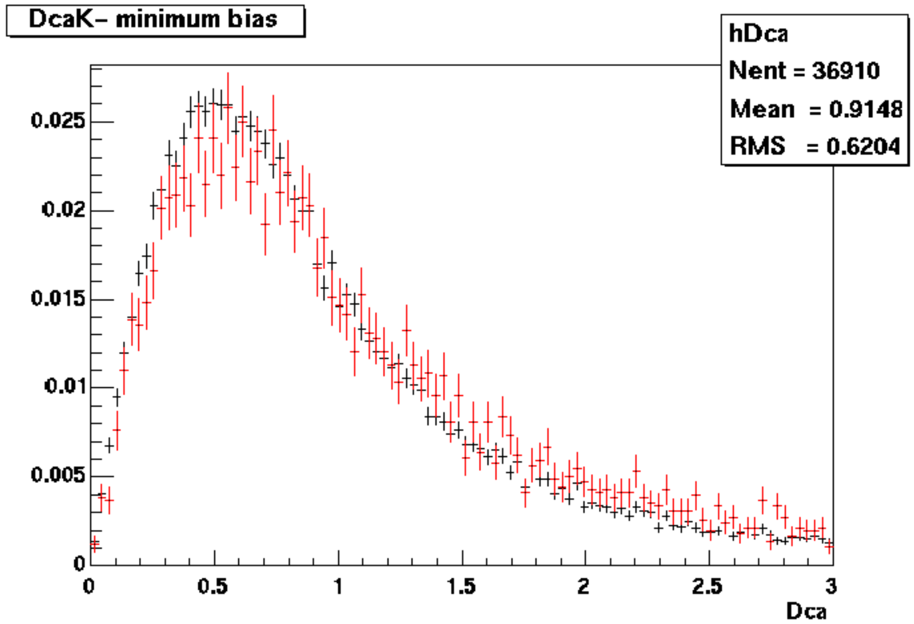

Figure 23: Comparison of DCA distribution between data (dark points) and MC (light points). For minimum bias they match as can be seen on the picture. The same comparison was made for different p_t cuts and different centrality bins and a match was found in all cases.

• $Nhits \geq 25$

• $|DCA| < 3cm$

We used both central and minimum bias triggers in our analysis. We used 71,000 minimun bias events and 39,000 central events. The data were divided into 8 centrality bins corresponding to a fraction of the measured cross-section of the charged particle multiplicity distribution, with bin 1 being the most peripheral and bin 8 corresponding to the most central collisions. To make sure the charged particles were within the TPC a cut of $|\eta| < 0.5$ was required (the TPC has an angular coverage of $|\eta| < 0.88$). Table 2 shows the cuts on N_{ch} as well as the percentage range to which they correspond, that were used to assign centrality bins.

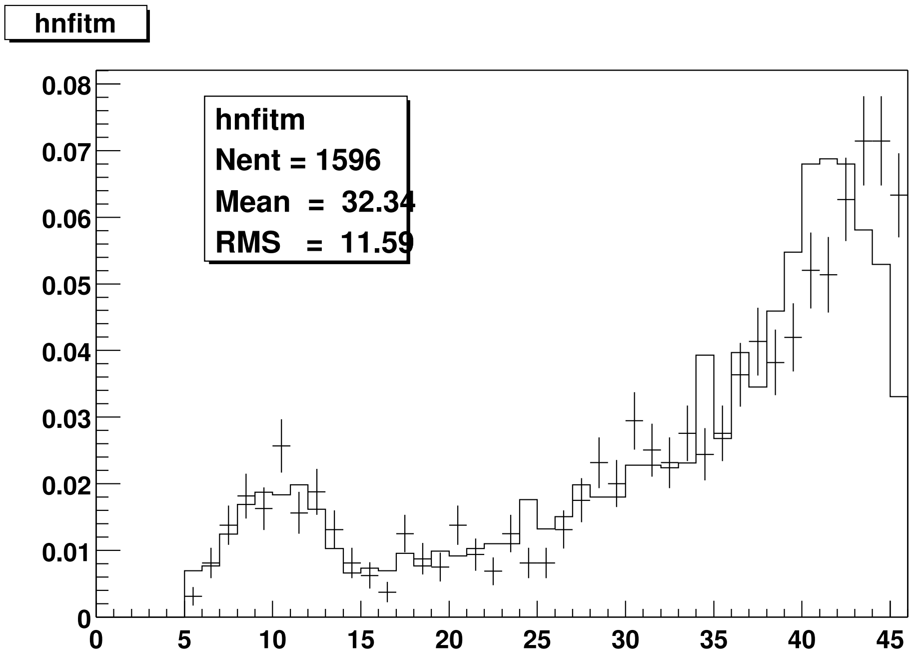

Figure 24: Comparison on the number of fit points from MC (points) with data (histogram) showing the agreement.

Table 2: Centrality bins definition

Bin	N_{ch} Range	Percentage Range
1	13-66	58%-85%
2	67-120	45%-58%
3	121-180	34%-45%
4	181-240	26%-34%
5	241-306	18%-26%
6	307-373	11%-18%
7	374-440	6%-18%
8	441-	0%-6%

3.3 Kaon Identification

The first step in the study of kaon spectra is to identify them, so they can be separated from the other species of particles produced in the fireball. To achieve this goal, we use the TPC capability to separate different species of particles via energy loss (dE/dx). Relativistic charged particles lose energy in the TPC gas by ionization. For the same momentum this energy loss rate is slightly different for each species of particles, as shown in figure (25). In this figure we can see how at low momentum, we can differentiate the different kinds of particles. However, at higher momentum, the dE/dx of all particles converge to make the identification process more difficult. In order to identify kaons above 0.6 GeV/c, we need to understand them at lower momenta and then extrapolate their behaviour. However, not even this extrapolation technique works for momenta higher than 0.8 GeV/c where they merge significantly with pions. Understanding the shape of the dE/dx curve is therefore of great importance. This theoretical dE/dx curve is given by the Bethe-Bloch equation:

$$-\frac{dE}{dx} = Kz^2\frac{Z}{A}\frac{1}{\beta^2}[0.5ln\frac{2m_ec^2\beta^2\gamma^2T_{max}}{I^2} - \beta^2 - 0.5\delta] \tag{56}$$

In this equation, T_{max} is the maximum kinetic energy that a free electron can receive in a collision with an incident particle. The variable I is the mean excitation energy of the medium. The variables A and Z are the usual atomic mass and atomic number of the medium. The variable z is the atomic number of the incident particles. The variable δ is the density effect correction to ionization energy loss. The variables β and γ have their usual relativistic kinematic definitions pertaining to the incident particle. K is defined as $4\pi N_Ar_e^2m_ec^2$. Here N_A and r_e are Avogadro's number and

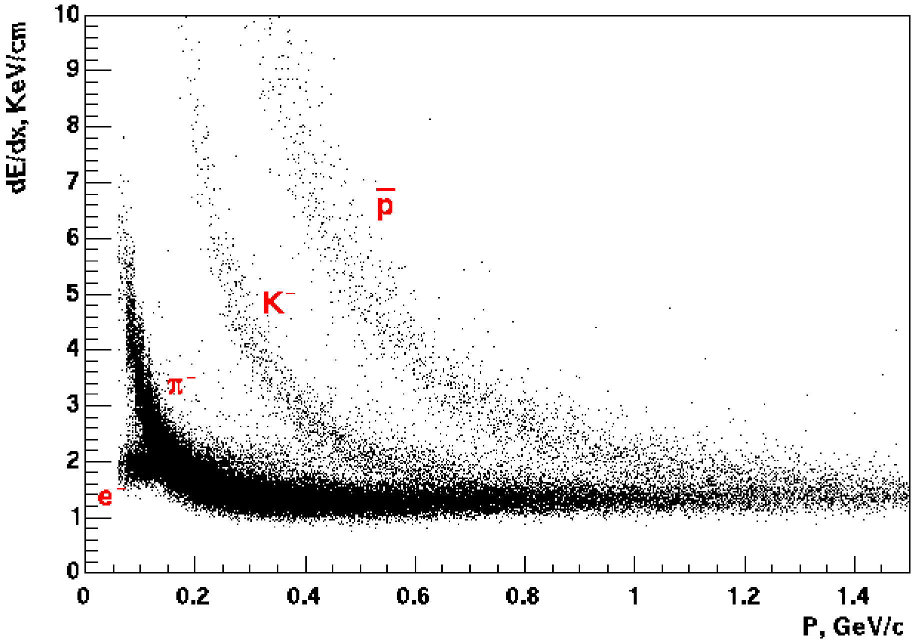

Figure 25: Energy loss (dE/dx) vs p: Particle identification in the TPC is achieved by the different energy loss rate of of different species of particles. Notice that the kaon band can be distinguished up to a momentum of about 0.6 GeV/c.

the classical electron radius respectively. To a good approximation in the momentum range we are studying, the Bethe-Bloch equation for kaons can be reduced to:

$$-\frac{dE}{dx} = \frac{1.15 * 10^{-6}}{\beta^2} \tag{57}$$

which will be used on the next step.

3.4 The z Variable

Kaon identification using measured dE/dx can be simplified even further by introducing a new variable called "z". Let's define z as:

$$z = ln(\frac{dE/dx}{BB}) \tag{58}$$

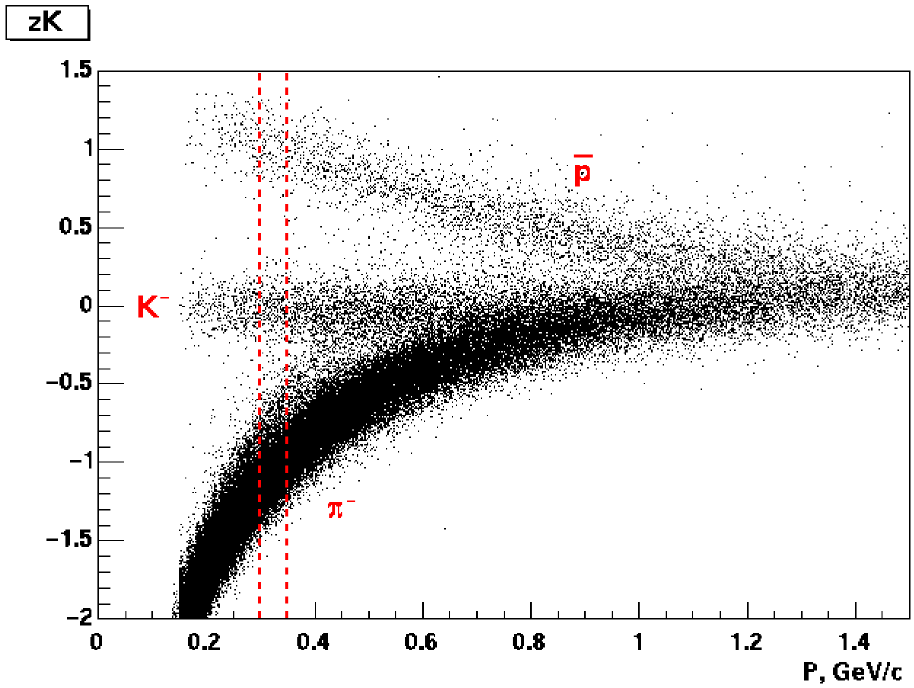

Figure 26: Energy loss in terms of the z variable. The kaon band is centered at z=0 which makes its identification easier once it is fitted to a gaussian.

where BB stands for Bethe-Bloch equation for kaons (equation 57). Notice that the value of z will approach zero for the kaon band since the numerator and the denominator are nearly equal. We can plot now dE/dx in terms of the z variable (figure 26). The z variable has the advantage that now we know the kaon band is centered around zero. Knowing the location of the kaons will be useful on our next step which is the fitting to gaussians.

3.5 Spectra

The next step to obtain the charged kaon spectra is to fit the z variable to 4 gaussians. We take each centrality bin and we split them into 20 p_t bins from 0 to 1

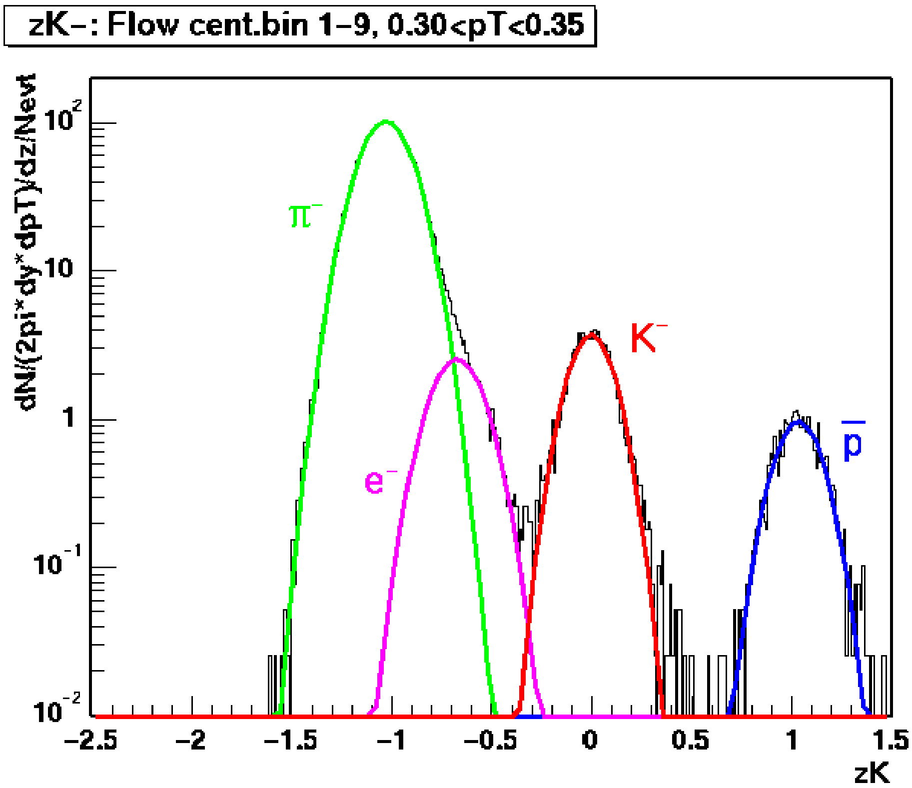

Figure 27: Fitting of z to gaussians. Notice that the kaon gaussian is centered at z=0. The area under the gaussian is proportional to the yield.

GeV. Then each one of these slices of z is projected into the y axis. This projection is then fitted to 4 gaussian curves: one for kaons, one for pions, one for (anti)protons and one for electrons (positrons). Figure 27 shows how the fitting looks like. Because each gaussian has 3 parameters (amplitude, width and centroid location), we could get a total of 12 parameters. These 12 parameters are very important because they are needed to obtain the area under each gaussian which is proportional to the yield.

The process of extracting the kaon yields involved the analysis of several of those 12 parameters. However this process can be summarized in four steps:

•Fix the width of the gaussians.

•Parametrization of the electron (positron) dE/dx to take into account the relativistic rise effect.

•Parametrization of the electron (positron) yield.

•Fit the kaon spectra to an exponential in m_t to extract the yields and inverse slope parameters.

All these steps are shown in the figures below. All figures have p_t on the horizontal axis. Figure 28 shows the width of the gaussian peaks. At $p_t < 0.5$ GeV/c the width of the electrons are set to be equal to the width of the pions (crosses). This is done because the widths of the peak depends on the detector resolution and in theory they should be equal. However the kaons (circles) and proton (filled squares) widths are not fixed. We follow this procedure because in that region, pions and electrons (positrons) merge. In the $0.5 < p_t < 0.7$ GeV/c range, all widths, except the proton's, are set to be equal to each other. This is done because now the kaons merge while the protons remain isolated. In the range of $0.7 < p_t < 0.8$ GeV/c we neglect the electron (positron) contribution since most electrons are at low momenta.

Figure 29 is the centroid (dE/dx) distribution of the 4 species of particles. Notice how at medium p_t we parametrize the electron dE/dx to take into account the effect of relativistic rising. The parametrization curve was obtained from Monte Carlo simulations and it is equal to:

$$dE/dx = (2.54 + 0.131 log(p_t)) \tag{59}$$

Understanding the electron contamination is one of the most important aspects of the analysis because when they merge with the kaons they make the yields higher than

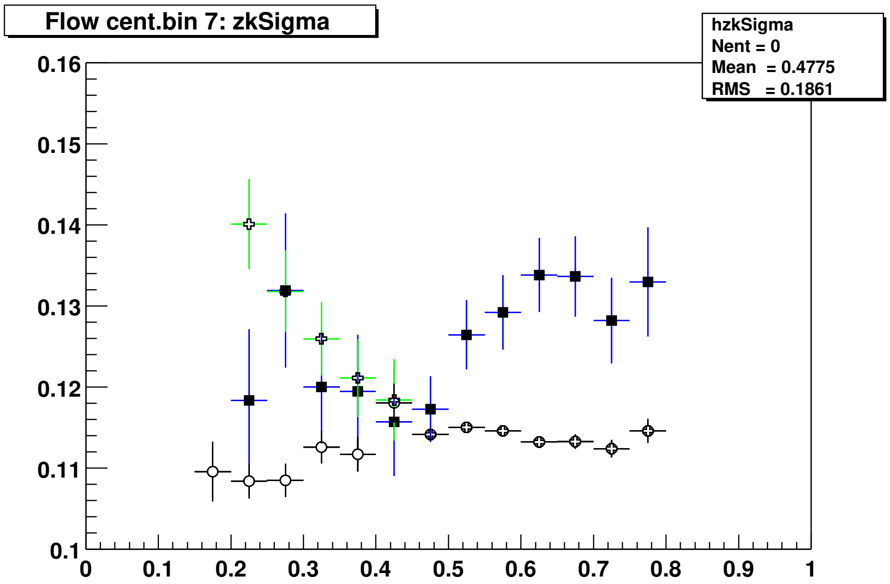

Figure 28: Widths of the gaussians. Widths are required to obtain the area of the gaussian, and hence the yields. Crosses are pions, circles are kaons and filled squares are protons. Notice how kaons and pions are superimpossed above 0.5 GeV/c, while (anti)protons remain separate. See text for explanation.

what they really are. Therefore we must substract the electron background to obtain the correct kaon yields.

Figure 31 shows the raw kaon (circles) and electron spectra. To be more specific, we are plotting $dN/(2\pi dydp_t)$. Notice that at high p_t the electron spectra is fixed (no error bars). The reason for doing this is to get rid of the electron contamination using a procedure that will be explained below. Figure 32 shows the ratio of the electron spectra to the kaon spectra, where we observe a 10% electron contribution to the kaon yield at high p_t.

Once we have the raw spectra, the next step is to obtain the corrected spectra of kaons. As mentioned before, in order to achieve this we have to get rid of the electron (positron) contamination. We do it by fixing the electron (positron) yield

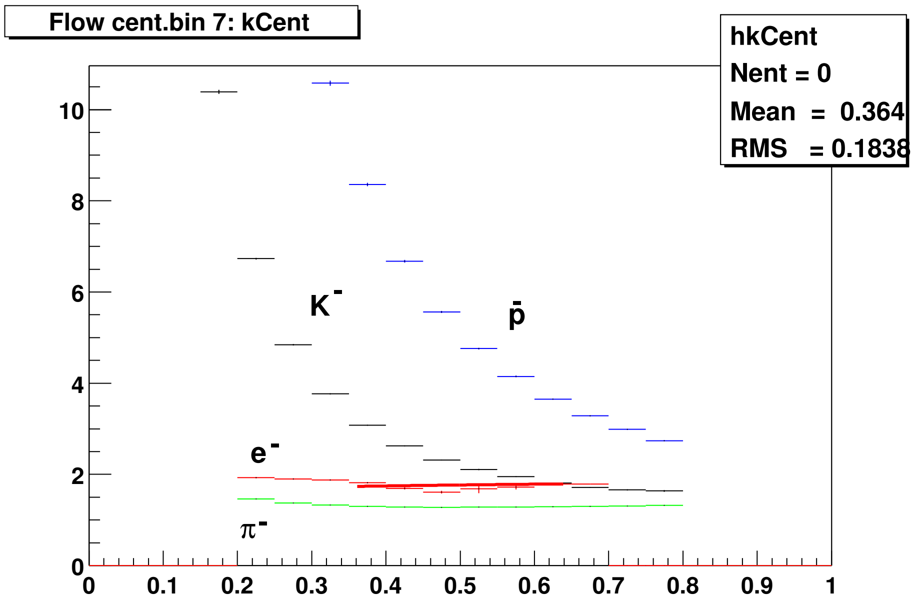

Figure 29: Centroids of the four gaussians. This is basically the dE/dx. Notice the portion of the electron band fixed to take into account the effect of relativistic rise. See text for explanation.

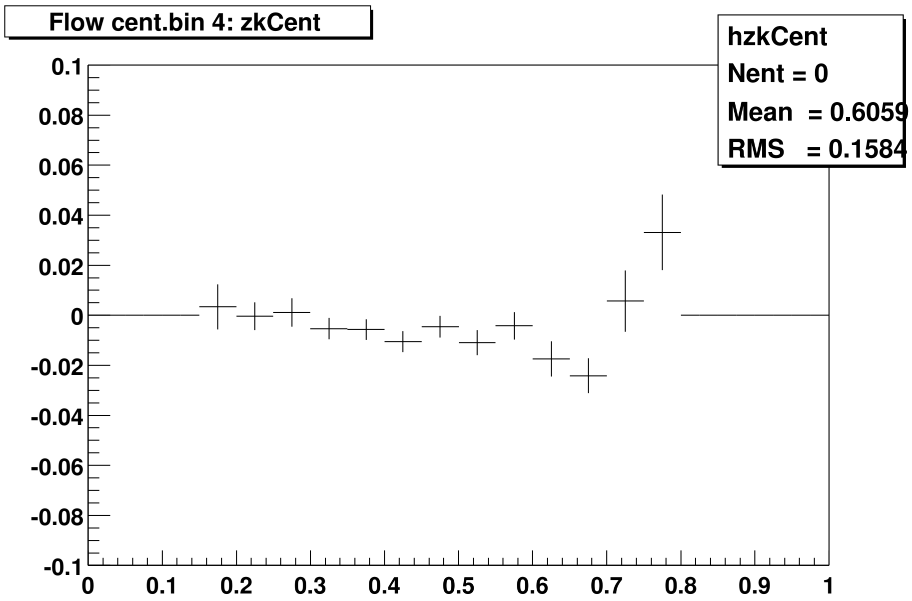

Figure 30: Kaon centroid in terms of z. It is centered around zero based on the definition of z.

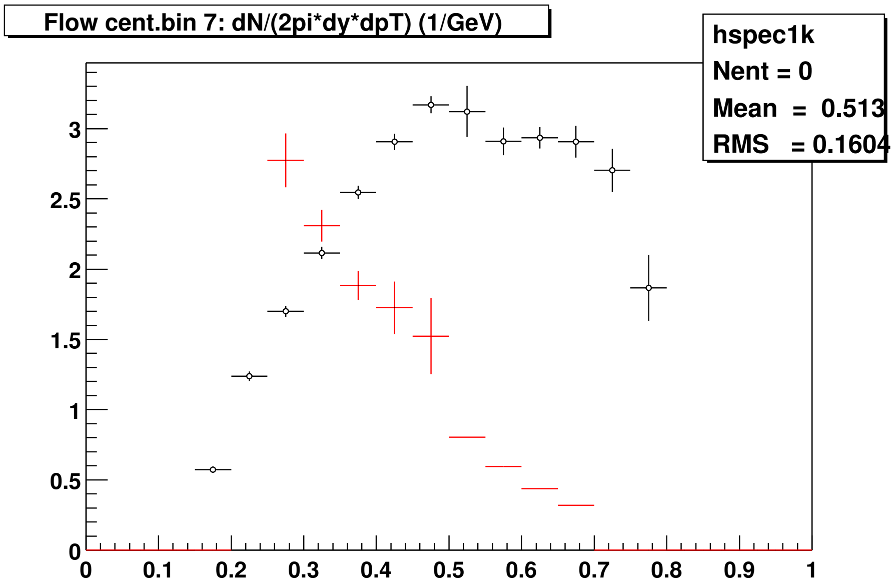

Figure 31: Raw spectra: circles are kaons, lines are electrons. At high p_t electrons are fixed to get rid of contamination to the kaons.

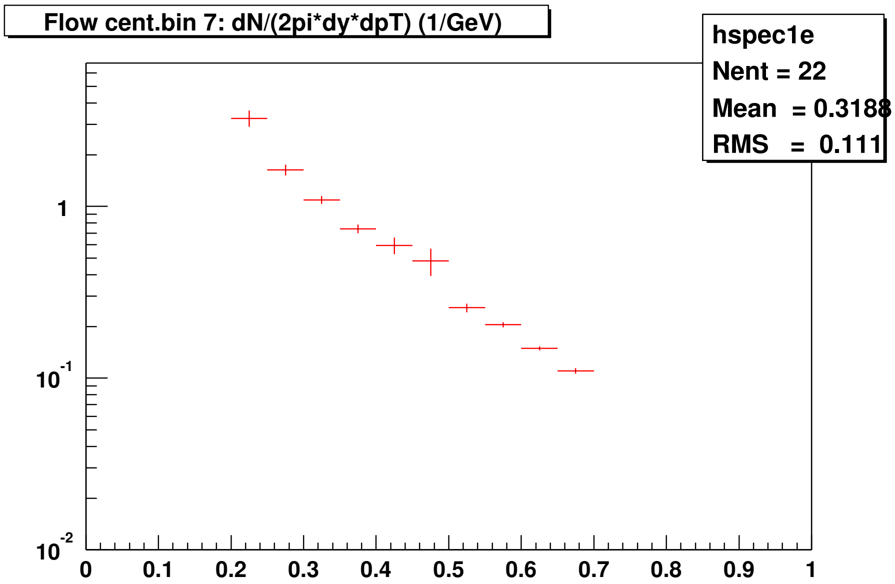

Figure 32: Ratio of raw spectra of electrons to raw spectra of kaon. Notice that in the region where they merge, at around 0.6 GeV/c, electrons contribute to the kaon peak by about 10%.

where necessary. For $p_t < 0.5$ GeV/c where kaons are separated from other species, we don't make corrections due to electron (positron) contamination. Here we estimated a point-to-point systematic error of 5%. In the range $0.5 < p_t < 0.7$ GeV/c where kaons and electrons (positrons) merge, we parametrize the electron (positron) yield at low p_t and use the result to fix the yield. Here we estimated a point-to-point systematic error of 10%. Finally, in the range $0.7 < p_t < 0.8$ GeV/c we neglect the electron (positron) contribution by setting their yield to be equal to 0. This is possible for two reasons: first, most electrons and positrons are at low momenta, and second, in this range the electron (positron) band begins to separate from the kaon band due to the relativistic rise effect (see figure 29). In this last region our estimated systematic error is 15%. We also included an overall correlated systematic error of 5% in the 3 regions, and an additional 5% error due to uncertainties in our Monte Carlo determination of efficiencies (see section 3.6).

Figure (33) shows the corrected $dN/(2\pi dy p_t dp_t)$ of electrons (positrons) as circles, and kaons as lines. The line across the low p_t electrons (positrons) is their parametrization. Then the high p_t electrons (positrons) are fixed to this parametrization so all electrons (positrons) follow the same trend as predicted by our simulations (see figure 34). Once the electron (positron) contamination is taken care of, the kaon spectra exhibit an exponential shape in m_t, therefore we fit it to the following function (equation 60), treating the integrated rapidity density dN/dy and the inverse slope parameter T as free parameters (p0 and p1 in figure 33 respectively).

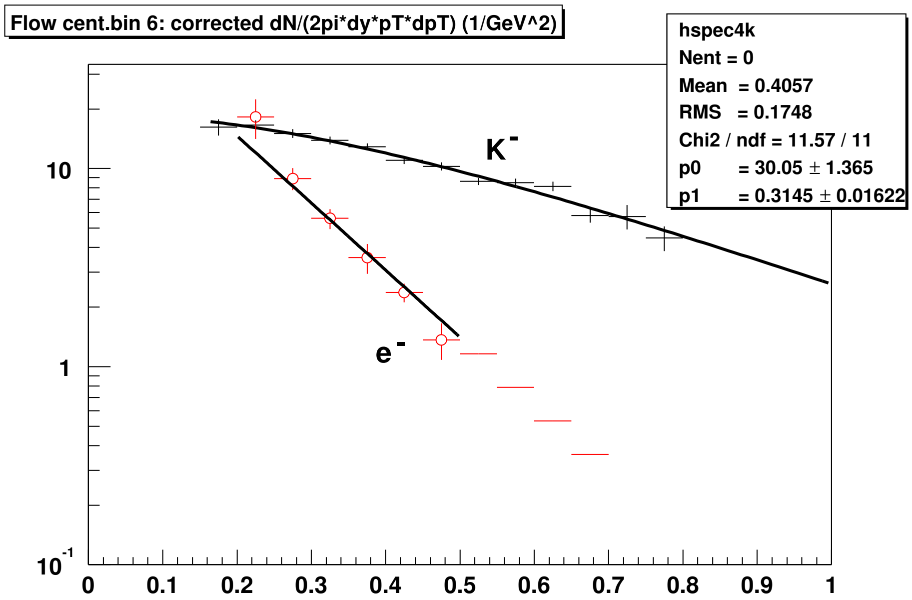

Figure 33: Corrected spectra. Kaons are fitted to an exponential in m_t as described on the text. The parameter p0 on the box represents the yield, while p1 is the inverse slope parameter. The circles are the electrons which yields are fixed at high p_t.

$$\frac{d^2N}{2\pi m_t dm_t dy} = \frac{dN/dy}{2\pi(T+m)T} exp(\frac{-(m_t - m)}{T}) \tag{60}$$

The final outcome of the analysis described above is that we obtain the charged kaon yield and the inverse slope parameter T from figure 33. We repeated the same analysis for all centrality bins and the results are reported on chapter 4.

3.6 Corrections for Efficiency

The raw yields obtained from the fittings, also had to be corrected to take into account tracking inefficiency, hadronic interaction loss, detector acceptance and decays. We used Monte Carlo (MC) embedded data to obtain the efficiency that included all these factors. In the embedding procedure we take a real event and embed MC

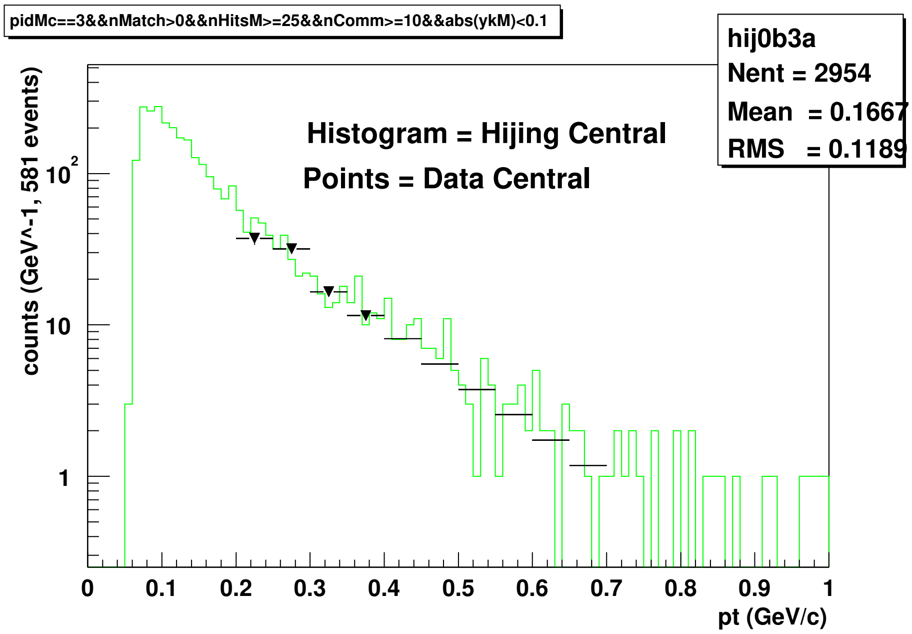

Figure 34: Comparison between data and MC of the electron yield where the agreement can be seen. Understanding the electron (positron) contamination is very important for our analysis for reasons described on the text.

tracks into the raw data file. Our simulation is obtained used the GEANT MC. This simulation is then processed through our reconstruction software chain. The ratio of the reconstructed tracks to the input embedded tracks is the efficiency. The efficiency versus tranverse momentum plot is shown in figure (35) for K^- and figure (36) for K^+. The efficiencies follow an exponential trend and we fit them to obtain expression. The fitting gives us mathematical forms of the efficiencies as a function of tranverse momentum for K^- and K^+ respectively:

$$\epsilon = 0.671exp(-(\frac{.219}{p_t})^{1.765}) \tag{61}$$

$$\epsilon = 0.664exp(-(\frac{.211}{p_t})^{1.793}) \tag{62}$$

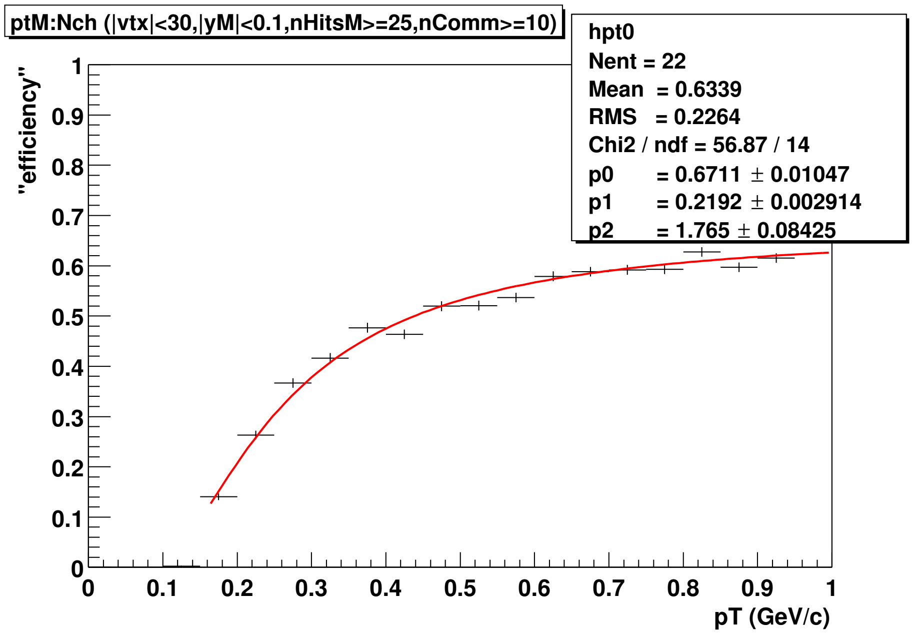

Figure 35: Efficiency for K-.

The efficiency of K^- is expected to be around 1% larger than the efficiency of K^+. This difference arises from the absorption loss in the detector materials. The probability of survival for a kaon in the material is given by:

$$P = exp(-\sigma * N_A * \rho * L * p/p_t) \tag{63}$$

where σ is the cross section, N_A is Avogadro constant, ρ is the density of the material, and L is the distance between the beam axis and the edge of the TPC. Because the exponential is very small, the probability can be approximated into:

$$P \approx 1 - \sigma * N_A * \rho * L * p/p_t \tag{64}$$

And the absorption loss is just 1-P, so it is given by:

$$Absorption = \sigma * N_A * \rho * L * p/p_t \tag{65}$$

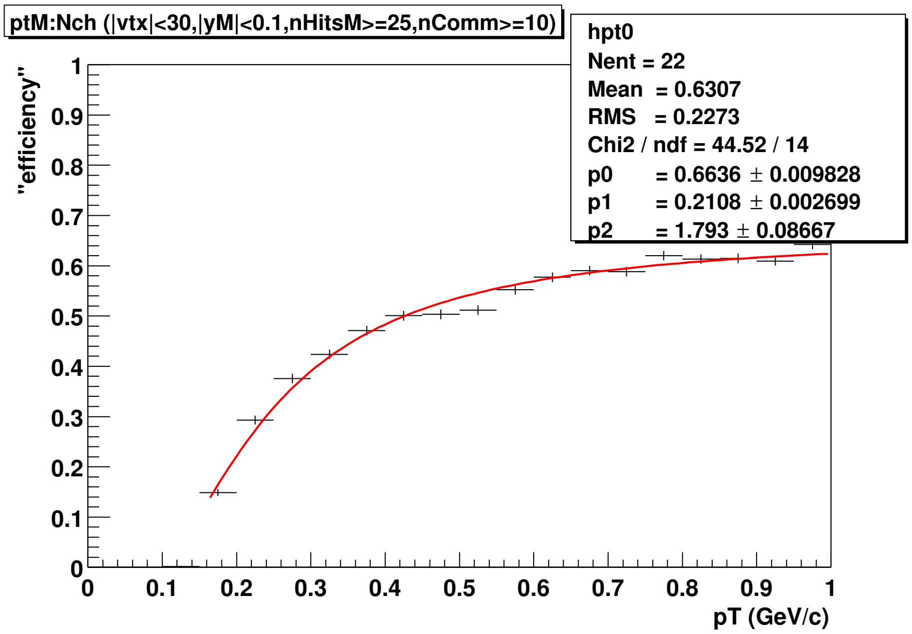

Figure 36: Efficiency for K+.

We can now plug in some numbers. The $L\rho$ for the TPC materials are $0.18 g/cm^2$ for the Be beam pipe, $0.05 g/cm^2$ for the air between the beam pipe and the inner field cage, $0.24 g/cm^2$ for the inner field cage, and $0.23 g/cm^2$ for the P10 gas. Adding them we obtain a total $L\rho = 0.7 g/cm^2$. The cross section for the K^- is around 30mb. Finally at mid-rapidity $p/p_t \approx 1$. Plugging all these numbers into equation (65), we get an absorption around 1%. For the K^+ the numbers are similar, but the cross section is about 5 times smaller, making the absorption negligible. We can verify this effect by taking the ratio of the efficiency curves. Figure (37) is this ratio and we observe that the fitting gives us a 1% difference as expected (see value p0 on box).

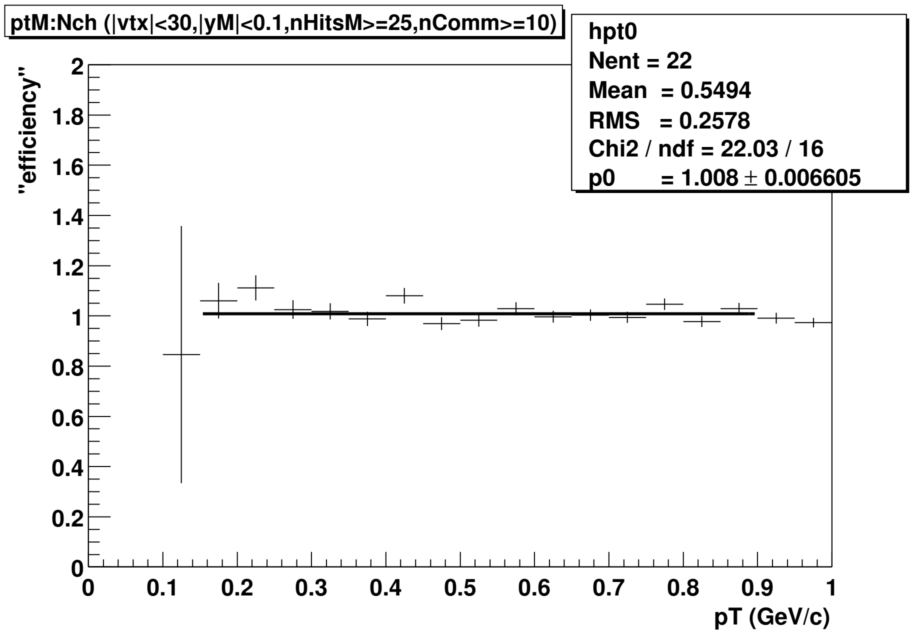

Figure 37: Efficiencies ratio: this is the ratio of the previous two plots. The parameter p0 on the box is the value of the fitting function (solid line). Notice the 1% difference explained on the text.

3.7 Energy Loss Correction

We also perform energy loss correction to select the z vertex cut mentioned on section 3.2. We started by looking at the energy loss as a function of p_t. Figure (38) shows the difference between the reconstructed and the MC p_t as a function of the MC p_t for $|z| < 100cm$. The 3 bands we observe can be explain by the different z position of the event vertex. To pinpoint the z vertex cut that causes this effect we looked at the energy loss as a function of z vertex (figure 39) and we notice 3 regions: central region, at $|z| < 35cm$; outer region, at $|z| > 55cm$; and the separation region at $35cm < |z| < 55cm$. In this separation region the energy loss is the worst which is probably due to the material in the TPC. To avoid the complications of this region, we selected our cut at 30 cm. Once we have our cut, we can replot the energy loss as a function of p_t (see figure 40) where we don't see the problem anymore.

The particle energy loss can be corrected on average as follows:

$$dE = -dE_{min} * p/p_t/\beta^2 \tag{66}$$

where dE_{min} is the energy loss of minimum ionizing particles tranversing perpendicular to the beam pipe. Also, since the momentum loss is proportional to the tranverse momentum loss, then $dp/p = dp_t/p_t$ which leads to:

$$dp_t = p_t \frac{dp}{p} = -p_t \frac{EdE}{p^2} = \frac{dE_{min}}{\beta^3} \tag{67}$$

The average energy loss can be fitted to the functional form (solid line on figure 40):

$$dp_t = -dE_{min}/\beta^a \tag{68}$$

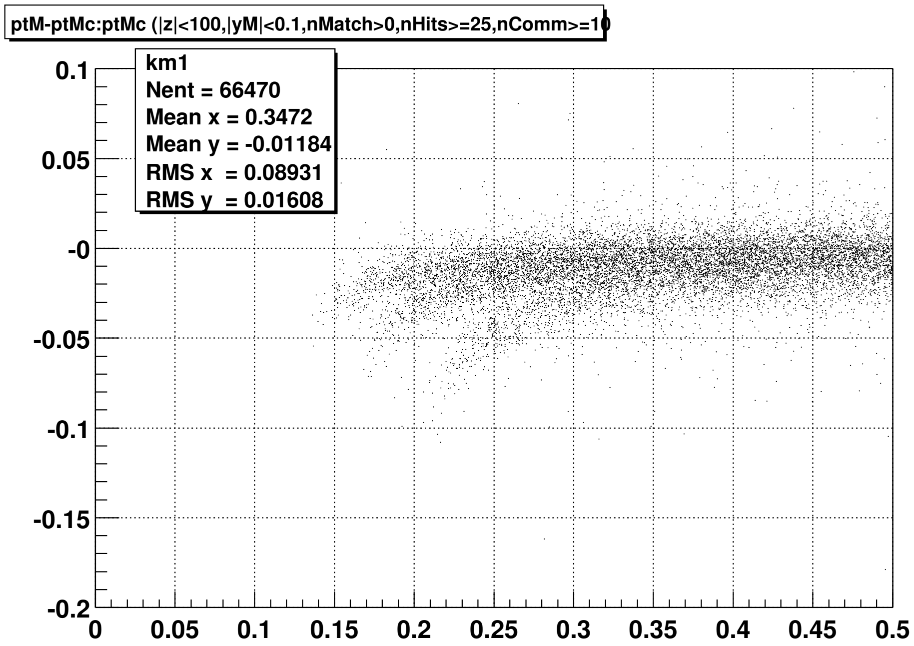

Figure 38: Energy loss as a function of p_t for $|z| < 100$.

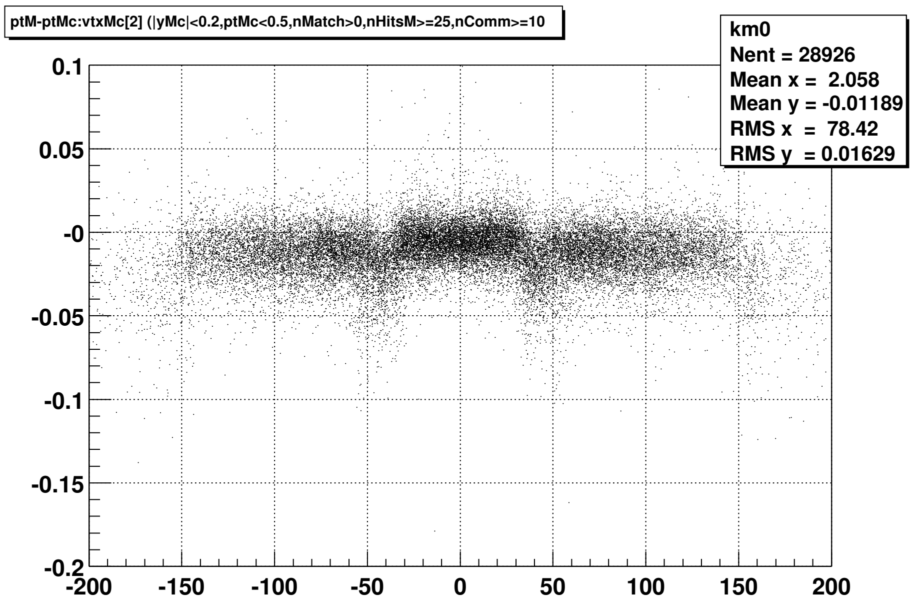

Figure 39: Energy loss as a function of z vertex. See text for an explanation of the three regions and how they were used to determine the z vertex cut.

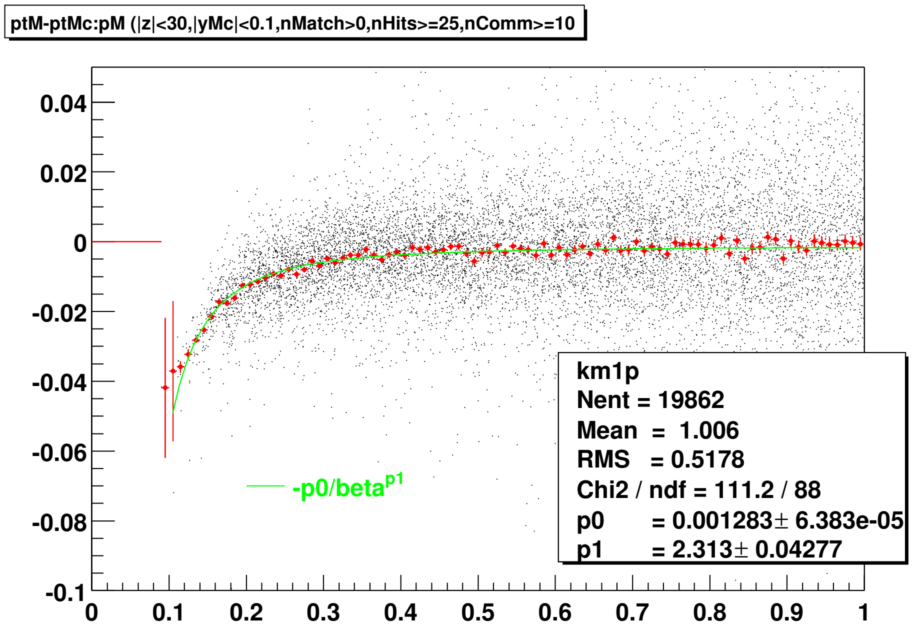

Figure 40: Energy loss as a function of p_t for $|z| < 30$.

In the figure the p0 fitting parameter correspond to the dE_{min}. The other free parameter, p1, is the power factor "a" to which β is raised. The reason "a" is treated as a free parameter is because β is calculated using the reconstructed momentum after energy loss in the beam pipe and the TPC inner cage. This will make β from equation (67) bigger than β from equation (68), therefore in order to make the correction, "a" will be less than 3. Looking at the numbers in figure (40), we obtain a energy loss equal to:

$$dp_t = -0.00128/\beta^{2.313}. \tag{69}$$

This energy loss correction should be applied by making the following changes:

$$dp_t \rightarrow dp_t + \frac{dE_{min}}{\beta^a} \tag{70}$$

and

$$dp_z \rightarrow dp_z + \frac{dE_{min}}{\beta^a}\frac{p_z}{p_t}. \tag{71}$$

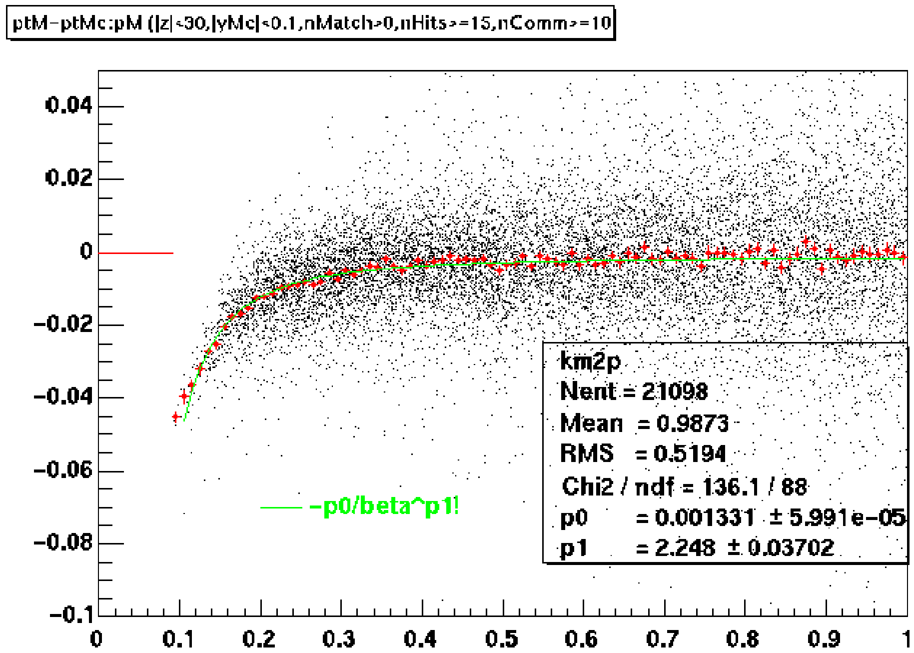

Figure 41: Energy loss as a function of p_t for $Nhits > 15$.

We also have to check to see if there is any dependence of the energy loss on the number of hits. We do not expect to see much dependence because the energy loss in the TPC gas is very small, since most of it occurs in the inner field cage and the beam pipe. To check this, we replot figure (40) now with number of hits greater than 15 and 35 (instead of 25) and do a fitting again. Figures (41) and (42) give us the numbers and we observe they are nearly identical. A comparison of these sets of number can be seen on table 3, while figures (40,41,42) are superimpossed on figure (43). After making this last correction to the spectra, we are now in position to obtain results.

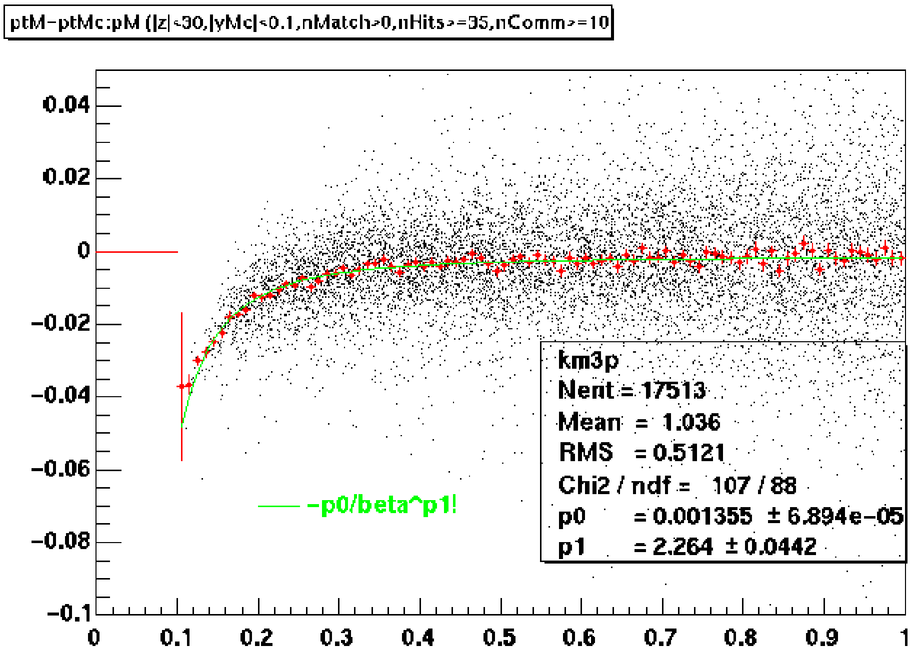

Figure 42: Energy loss as a function of p_t for $Nhits > 35$.

Table 3: Energy loss dependence on the number of hits. As can be seen from the numbers, there is no dependence.

Nhits greater than	dE_{min}	parameter "a"
15	0.001331	2.248
25	0.001283	2.313
35	0.001355	2.264

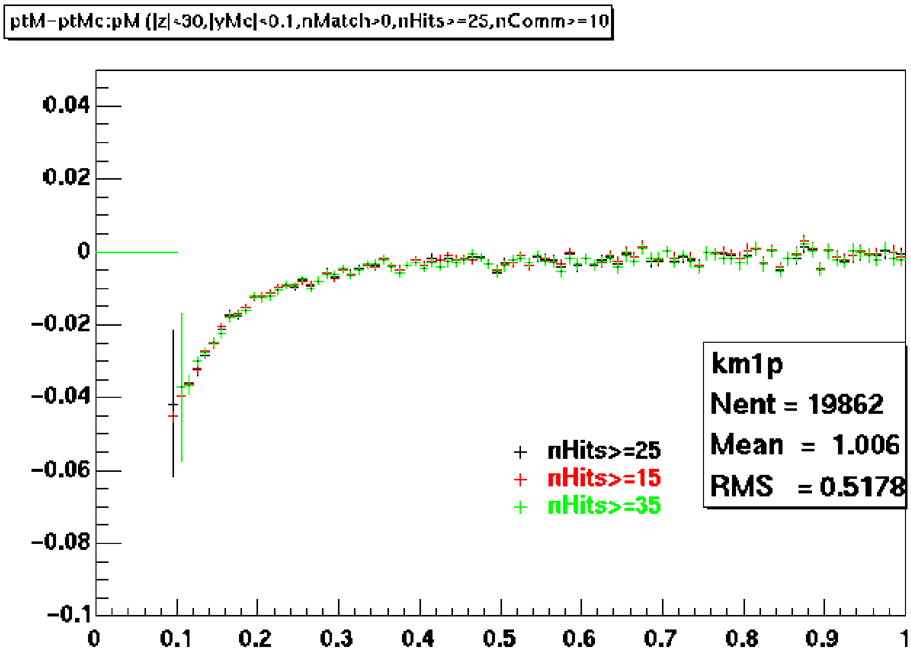

Figure 43: Comparison of the energy loss for different number of hits. There is no difference between them as can be seen on the numbers on table 3.

4 RESULTS

4.1 Kaon Yields and Ratios

As mentioned before, the purpose of studying charged kaon production was to observe strangeness enhancement over previous experiments [49-56]. Table 4 summarizes the charged kaon dN/dy and inverse slope parameters T for all centrality bins as obtained from the analysis described in the previous chapter (see equation 60). The errors shown on table 4 are combined statistical and uncorrelated systematic errors added in quadrature. An additional 10% and 8% correlated systematic errors are estimated for dN/dy and T respectively (see section 3.6). Table 4 also lists the average pseudo-rapidity density of negative hadrons $dN_{h^-}/d\eta$ as reported by STAR [57]. The tranverse mass spectra of the invariant yields is shown in figure (44) for selected centrality bins. As mentioned earlier, the spectra follows an exponential behavior in m_t (solid line).

The centrality dependence of our results can be seen on figure (45). In the top panel of figure (18) we see the inverse slope parameter T as a function of $dN_{h^-}/d\eta$ (centrality). For comparison, we also included the STAR results as analyzed via the decay topology method [58]. While K^+ and K^- have similar behavior, we do observe an increase in T with centrality from around 240 MeV to 300 MeV. The kaon inverse slope parameter is smaller than those of $\bar{p}$ [59], ϕ and Λ [60] measured at RHIC. This mass dependence agrees with the tranverse radial flow model described on [61] and [62] where T relates to the freeze out temperature T_{fo} according to:

$$T \approx T_{fo} + \frac{1}{2} m < \beta_t >^2 . \tag{72}$$

In this equation β_t can be identified with the averaged collective flow velocity. This expression is just a qualitative approximation which depends on the exact mechanism of expansion. We can also compared these results with the kaon inverse slope parameters from AGS and SPS [48-55]. At the AGS, for most central collisions, T = 200 MeV; and at the SPS, T = 240 MeV. The larger value of T at RHIC might be an indication of a larger radial flow velocity as mentioned above, or it could mean a larger T_{fo} from equation (72).

The enhancement of kaon production at RHIC can be better understood as the ratio of kaons to other particle species as a function of centrality and energy. We can then compare our results with those of previous experiments. In the lower panel of figure (45) we have plotted the kaon dN/dy to $dN_{h^-}/d\eta$ ratio as a function of $dN_{h^-}/d\eta$. This ratio is essentially constant across centrality which might indicate a similar strangeness production mechanism in peripheral and central collisions.

A more common way of determining a relative increase in charged kaon production is to compare the K/π ratio with those of previous experiments. In order to do that we need to deduce the dN/dy for negative pions from our knowledge of the yields of negative hadrons [57], antiprotons [59], and negative kaons obtained by our analysis.

Table 4: Summary of fitting results: Quoted errors are combined statistical and uncorrelated systematic errors; An additional 10% and 8% correlated systematic errors are estimated for dN/dy and T respectively.

Cent. Bin	$dN_{h^-}/d\eta$	K^+ dN/dy	T	K^- dN/dy	T
1	17.9	2.5 ± 0.1	238 ± 18	2.4 ± 0.1	235 ± 19
2	47.3	7.2 ± 0.5	248 ± 19	6.3 ± 0.4	257 ± 20
3	78.9	13.6 ± 0.9	299 ± 22	11.3 ± 0.7	266 ± 19
4	115	19.3 ± 1.6	322 ± 27	15.2 ± 0.9	264 ± 19
5	154	24.3 ± 1.8	296 ± 24	23.5 ± 1.9	317 ± 26
6	196	31.9 ± 2.2	301 ± 23	29.2 ± 2.3	306 ± 25
7	236	37.9 ± 2.1	297 ± 17	35.1 ± 2.1	296 ± 18
8	290	45.5 ± 2.2	282 ± 15	43.3 ± 2.3	296 ± 16

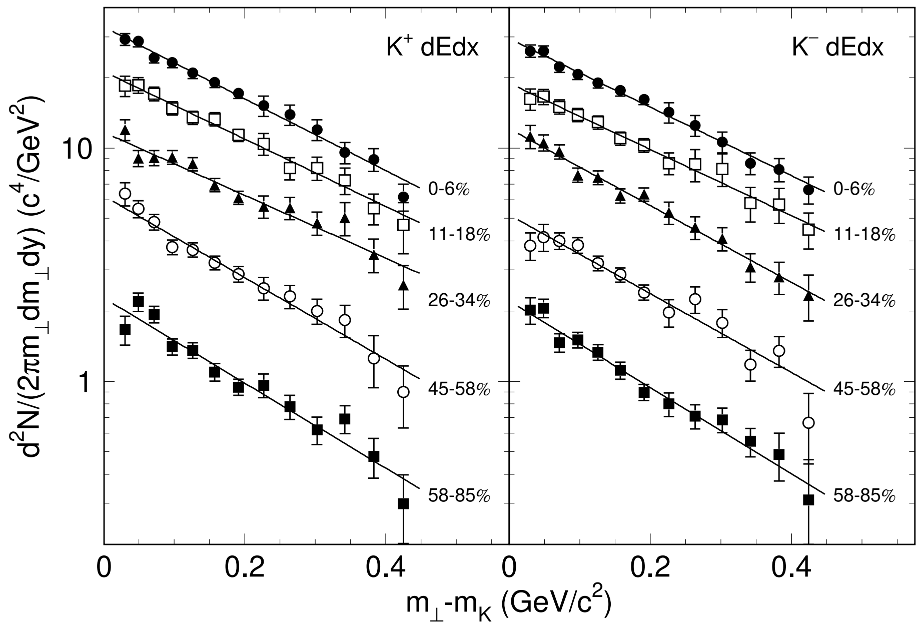

Figure 44: Charged kaon invariant yield tranverse mass spectra for selected centrality bins. Solid lines correspond to fitting to an exponential in m_t. Error bars are statistical. See text for description on systematic errors.

Since we know that:

$$\frac{dN_{h^-}}{d\eta} = \frac{dN_{\pi^-}}{d\eta} + \frac{dN_{K^-}}{d\eta} + \frac{dN_{\bar{p}}}{d\eta} \tag{73}$$

we need to obtain the pseudorapidity distribution for negative hadrons, antiprotons and K^- from the known rapidity distributions. The rapidity and pseudorapidity variables are related by:

$$\frac{dN}{d\eta} = \beta\frac{dN}{dy} \tag{74}$$

which can be used to relate our measured quantity to pseudorapidity (see section 3.5):

$$\frac{dN}{2\pi p_t d\eta dp_t} = \beta\frac{dN}{2\pi p_t dy dp_t}. \tag{75}$$

If we remember that:

$$\beta = \frac{p}{E} = \frac{p}{\sqrt{p^2 + m^2}} \tag{76}$$

which at mid-rapidity ($p = p_t$) becomes:

$$\beta = \frac{p_t}{\sqrt{p_t^2 + m^2}} \tag{77}$$

then we can substitute the right side of equation (75) by equation (77) and by our parametrization (equation 60) to obtain:

$$\frac{dN}{2\pi p_t d\eta dp_t} = \frac{p_t}{\sqrt{p_t^2 + m^2}}\frac{dN/dy}{2\pi(T+m)T}exp(\frac{-(m_t - m)}{T}) \tag{78}$$

which can be solved if we replace m_t by equation (26) and integrate both sides with respect to p_t:

$$\frac{dN}{d\eta} = \int \frac{p_t^2}{\sqrt{p_t^2 + m^2}}\frac{dN/dy}{(T+m)T}exp(\frac{-(\sqrt{p_t^2 + m^2} - m)}{T})dp_t. \tag{79}$$

The integral on the right side of this equation was solved numerically, giving us the conversion factor between rapidity and pseudorapidity. Our obtained values of the dN/dy for negative pions were consistent with preliminary measurements made by STAR [63-64] for different centrality bins. For the most central events we find $K^+/\pi^- = 0.16 \pm 0.01 \pm 0.02$ and $K^-/\pi^- = 0.15 \pm 0.01 \pm 0.02$. This ratios are nearly constant across all centrality bins which is in contrast to AGS and SPS [49-56]. We also notice that the following ratio:

$$\frac{K^+/\pi^-}{K^-/\pi^-} = \frac{K^+}{K^-} \tag{80}$$

is also constant as a function of centrality, as observed by previous experiment.

After the centrality dependence was studied, our next step is to look at the energy dependence. We start by plotting the K^-/π^- ratio as a function of $\sqrt{s}$ in figure (46). Since according to PHOBOS [65], the ratio of $\pi^-/\pi^+ = 1.00 \pm 0.01 \pm 0.02$ at mid-rapidity at RHIC, then our measured K^+/π^- can be taken to be equal to K^+/π^+ at mid-rapidity, which is also plotted on the same picture. The first thing we observed is that both K^+/π^+ and K^-/π^- ratios are enhanced by 50% with respect p+p [66-67] and p+$\bar{p}$ collisions [68] at similar energies. We also noticed that while K^-/π^- increases monotonically with $\sqrt{s}$, K^+/π^+ reaches a maximum at around $\sqrt{s} = 10$ GeV and then drops. This might indicate the K^+/π^+ dependence on the net baryon density which changes with energy [69-73]. This is the case because as mentioned on section 3.1, the K^+ is made of the $u\bar{s}$ quarks and the K^- is made of $\bar{u}s$ quarks. Since the colliding beams are made of protons (uud) and neutron (udd), there is a net number of up quarks to start the process. Therefore, we know that all anti-up, strange and anti-strange quarks are formed in the intial fireball, while the up quarks can come from either the colliding nuclei or they could have been created in the fireball. Since

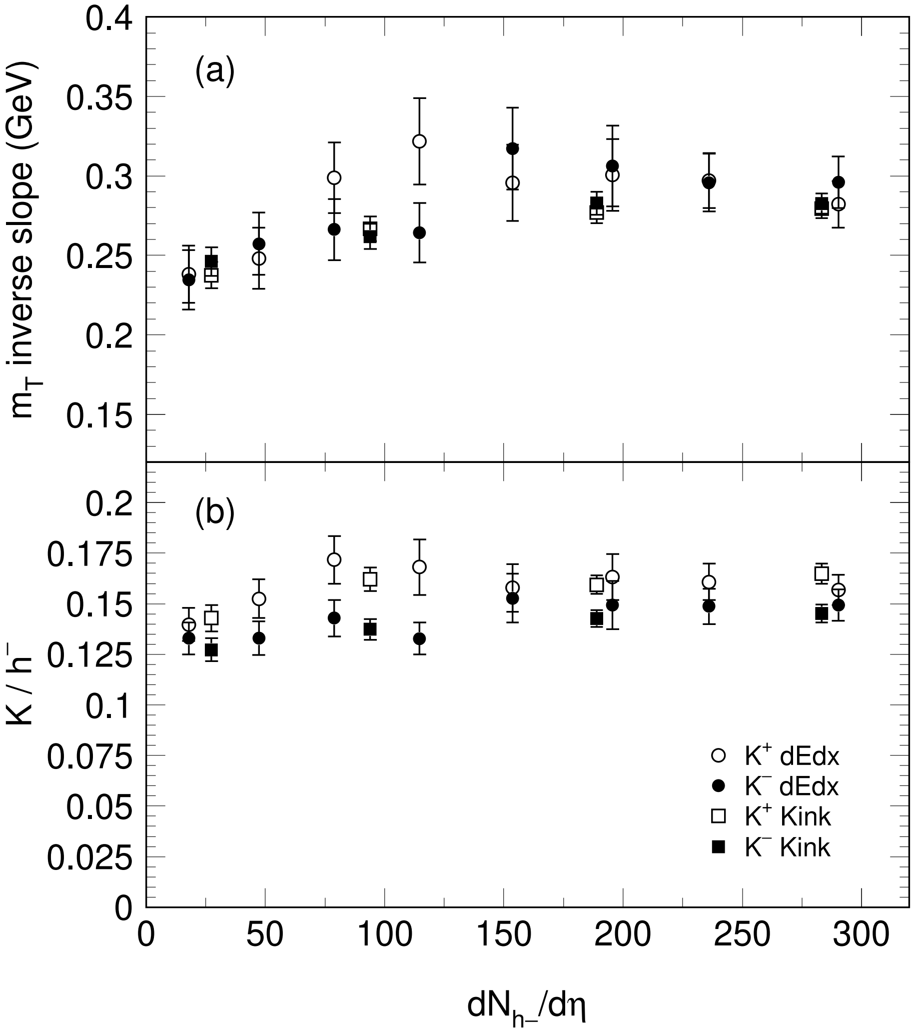

Figure 45: Centrality dependence: (a) of kaon inverse slope parameter and (b) the kaon to negative hadron ratio. Kink results are also shown to demonstrate agreement between two methods.

we want to study the strangeness production from the QCD vacuum we should focus on K^- which we know were made up completely from quarks produced in the QCD vacuum. In the lower panel of figure (46) we see the K^+/K^- ratio as a function of energy. This ratio is indicative of the relative contribution of associated to pair production. As mentioned before, with increasing energy, the net baryon density decreases [69-73] and thus the associated production of K^+ also decreases, while pair production increases due to gluon-gluon fusion into strange quark-antiquark pairs [26,28].

4.2 Omega Variable

In this section, motivated by the gluon saturation picture described in section 1.7, we would like to focus our attention to a new experimental variable called ω. This variable can be seen as the pion tranverse energy density. We start with the experimental observation that K^-/π^- increases with collision energy and so we define an ω_{cent} for central collisions as:

$$\omega_{cent} = 3 < m_t >_{cent} \frac{dN^{cent}_{<\pi>}/dy|_{y=0}}{\pi R^2} \tag{81}$$

where $dN^{cent}_{<\pi>}/dy)|_{y=0}$ is the pion density in central collisions at mid-rapidity, and R is the radius of the colliding nuclei. We now recognize from equation (28) that:

$$\omega_{cent} = (\epsilon \cdot \tau)_{cent} \tag{82}$$

that is the Bjorken energy density times the hadronic formation time. This is equiva-

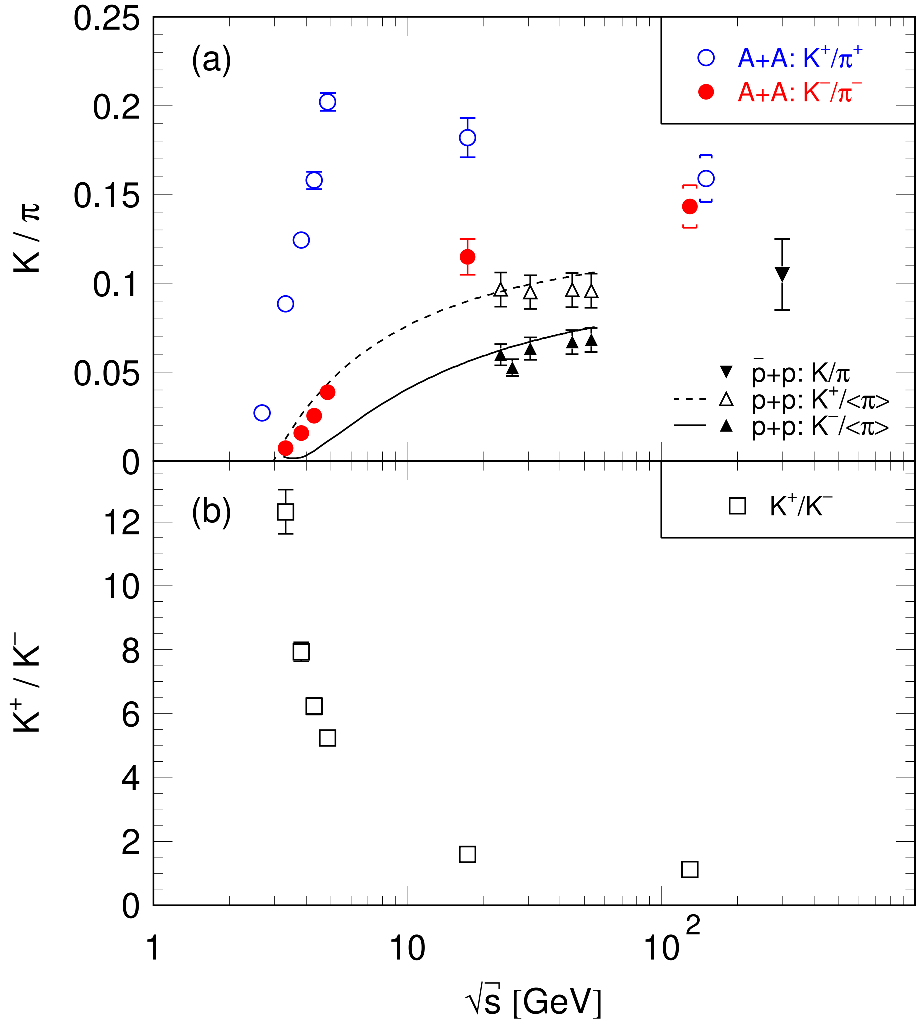

Figure 46: Energy dependence of (a) K/π ratios and (b) K^+/K^-. The curves on (a) are parametrization to p+p data. Also on (a), systematic errors of the STAR data are indicated by caps. See text for explanation.

lent to the tranverse area energy density in central collisions at the time of hadronization.

The second experimental observation we take into account is that K^-/π^- also increases with collision centrality at the AGS and SPS energies [74-76]. Therefore we include a term to account for centrality. Now ω becomes:

$$\omega = \omega_{cent}[\frac{< m_t >}{< m_t >^{cent}}(\frac{dN_{<\pi>}/dy}{dN^{cent}_{<\pi>}/dy})^{1/3}] \tag{83}$$

where the last term defines centrality. Notice that the last term will have a value of 0 for peripheral collisions and a value of 1 for central collisions. This equation can be rewritten as:

$$\omega = 3 < m_t >_{cent} \frac{(dN_{<\pi>}/dy)^{2/3}_{cent}}{\pi R^2}(dN_{<\pi>}/dy)^{1/3} \tag{84}$$

where R is the radius of the colliding nuclei. As mentioned above, this definition of ω is purely experimental. The $< m_t >$ term in equation (84) is related to the tranverse energy production. The second term in the ω definition depends on the collision energy: the larger the energy (smaller x), the larger the gluon density. The last term defines centrality: a larger number of nucleons on the longitudinal direction will increase the gluon tranverse density [77]. Since the pion multiplicity scales with the number of participants [77], and the volume of the fireball is also proportional to the number of participants, then:

$$\frac{(dN_{<\pi>}/dy)^{2/3}_{cent}}{\pi R^2} = \frac{(dN_{<\pi>}/dy)^{2/3}}{\pi r^2} \tag{85}$$

where r is the radius of the superimpossed region of the two nuclei, and now ω is reduced to:

$$\omega =< m_t > \frac{3dN_{<\pi>}/dy}{\pi r^2} \tag{86}$$

which gives as a result the following 2 relations:

$$\omega \propto Q_s^3 \tag{87}$$

and from equation (28):

$$\omega = \epsilon \cdot \tau \tag{88}$$

These relations lead us to believe that by studying ω we can learn something about the initial condition of the reactions. As mentioned in the previous section, the K^+/π^+ is not as useful because of its quark content, so we would like to focus on the K^-/π^- as a function of ω.

Figure (47) shows a plot of K^-/π^- versus ω, not only for the STAR data, but also for previous experiments. We observe that there is a linear increase for AGS and SPS energies, but it saturates at RHIC energy. Since ω is directly proportional to the gluon saturation scale Q_s, and to the energy density ϵ there are several physical interpretations of this phenomenon:

• Strangeness is produced mainly by gluon-gluon interactions, so K^- production is proportional to the gluon density squared (ρ^2). Since pion production is proportional to the gluon density(ρ), then the K^-/π^- ratio is then proportional to gluon density($\rho^2/\rho = \rho$). Since at RHIC we are probing very small x ($p_L/\sqrt{s}$) gluons, they

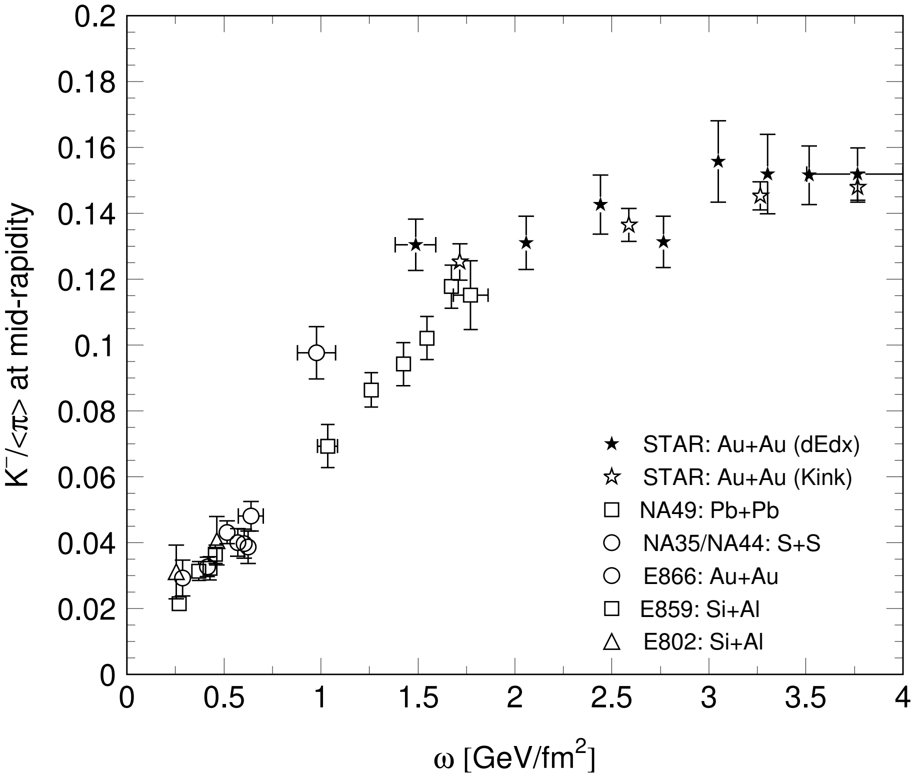

Figure 47: K^-/π vs ω: Notice how data from previous experiments increase linearly while STAR data points saturate. Possible explanations of this phenomenon are described on the text.

overlap in phase space hence gluon recombination occurs and thus we have gluon density saturation as described on chapter 1.

• From equation (87) ω is proportional to Q_s. At RHIC energy, the Q_s is much larger (2 GeV/c) than the strange quark mass so K^-/π^- will no longer be sensitive to ω. Another way to express it is that for a large Q_s the mass of the kaons and pions are virtually equal and they are produced at the same rate. This is not the case at SPS and AGS energies where gluons can be distinguished longitudinally and there is a significant contribution of quarks to the particle production.

• Another interpretation of figure (47) comes from equation (88). If we take τ to be a constant, then K^-/π^- is independent of the energy density. This could indicate that the chemical freeze-out condition which fixes this ratio is not sensitive to the initial energy density at RHIC.

All these possible scenarios for the physical meaning of figure (47) are speculative at this point. In order to gain more insight into the ω variable, further studies of K^-/π^- as a function of ω need to be done, especially in the overlap region with SPS (low energy RHIC points).

4.3 Summary and Discussion

In this thesis we have studied the charged kaon production in Au+Au collisions at mid-rapidity at $\sqrt{s}$ = 130 GeV seeking for a signature of QGP formation. We found that the spectra are well described by an exponential in tranverse mass. The inverse slope parameter T has a small dependence on centrality. The inverse slope parameters for kaons is smaller than those of $\bar{p}$, ψ and Λ. This mass dependence is consistent with tranverse radial flow. We also observe that the inverse slope parameter of kaons at RHIC energies is larger than at the AGS and the SPS, which may indicate a weaker radial flow at lower energies if this model is correct. The particles ratios do not depend on centrality, in contast with previous experiments. This tells us that the particle production mechanism is not significantly different from peripheral to central collisions. The K^-/π^- increases with energy while K^+/π^+ increases then decreases as a consequence of the net baryon density effect. The K^+/K^- decreases monotonically with energy, which indicates a reduction of net baryon density with energy, as expected. This ratio is also an indication of the reduction of associate kaon producion with respect pair production with energy, which is indicative of a larger strangeness production from gluon-gluon fusion into quark-antiquarks pairs. All these results combined, when compared with previous experiments, seem to be consistent with an enhancement in the strangeness production. Regarding the phenomenon of gluon saturation we observed that the K^-/π^- as a function of ω saturates at RHIC energies, which is not observed at the AGS and the SPS. This could be interpreted in several ways as described in the previous section. Of course further data is necessary and this picture will be more complete once the $\sqrt{s} = 200$ GeV and the lower energy data are analyzed. Even though our results are consistent with the creation of QGP, we cannot argue that QGP was indeed formed because in order to claim that we would require the observation of many other signatures, which are presently being studied by our collaborators. However, we are a step closer to fullfill the dreams of generations of scientists that have searched for the ultimate building blocks of matter, a dream that began 25 centuries ago.

BIBLIOGRAPHY

BIBLIOGRAPHY

[1] D.C. Lindberg, “The beginnings of western science”, The University of Chicago Press, Chicago (1992).

[2] R.S. Westfall, “The construction of modern science”, Cambridge University Press, Cambridge (1993).

[3] D.J.Griffiths, “Introduction to Elementary Particles”, Wiley, New York (1987).

[4] S. Hands, “The phase diagram of QCD”, Contemporary Phys. 42 (2001) 209-225.

[5] F. Karsch et al., “Flavor and quark mass dependence of QCD thermodynamics”, Nucl. Phys. Proc. Suppl. 94 (2001) 857-860.

[6] F. Karsch et al., “Quark mass and flavour dependence of the QCD phase transition”, Nucl. Phys. B605 (2001) 579-599.

[7] F. Karsch, “Lattice results on QCD thermodynamics”, Nucl. Phys. A698 (2002) 199-208.

[8] E. Laermann, “Recent results from lattice QCD simulations”, Nucl. Phys. A610 (1996) 1c.

[9] C.Y. Wong, “Introduction to High-Energy Heavy-Ion Collisions”, World Scientific Publishing, Singapore (1994).

[10] J.D. Bjorken, “Highly relativistic nucleus-nucleus collisions: The central rapidity region”, Phys. Rev. D 27 (1983) 140.

[11] L. Van Hove, “Hadronization model for quark-gluon plasma in ultra-relativistic collisions”, Z. Phys. C 27 (1985) 135-144.

[12] I.N. Mishustin, and J.I. Kapusta, “Collective deceleration of ultrarelativistic nuclei and creation of quark-gluon plasma”, Phys. Rev. Lett. 88 (2002) 112501.

[13] S.A. Bass et al., “Signatures of quark-gluon plasma formation in high energy heavy-ion collisions: a critical review”, J. Phys. G: Nucl. Part. Phys. 25 (1999) R1-R57.

[14] B.R. Schlei et al., “Predictions for $\sqrt{s} = 200A$ GeV Au+Au collisions from relativistic hydrodynamics”, Phys. Rev. C 59 (1999) R9-R12.

[15] P. Braun-Munzinger et al., “Probing the phase boundary between hadronic matter and the quark-gluon plasma in relativistic heavy-ion collisions”, Nucl. Phys. A 606 (1996) 320-328.

[16] P. Braun-Munzinger et al., “Dynamics of ultra-relativistic nuclear collisions with heavy beams: an experimental overview”, Nucl. Phys. A638 (1998) 3c-18c.

[17] S.A. Bass et al., “Dynamics of hot bulk QCD matter: From the quark-gluon plasma to hadronic freeze-out”, Phys. Rev. C 61 (2000) 064909(1-24).

[18] J. Rafelski, “Formation and observation of the quark-gluon plasma”, Phys. Reports 88 (1982) 331-347.

[19] I.N. Mishustin, “Nonequilibrium phase transition in rapidly expanding matter”, Phys. Rev. Lett. 82 (1999) 4779-4782.

[20] S.A. Bass et al., “Are we close to an equilibrated quark-gluon plasma? Nonequilibrium analysis of particle production in ultrarelativistic heavy ion collisions”, Phys. Rev. Lett. 81 (1998) 4092-4095.

[21] H. van Hecke et al., “Evidence of early multistrange hadron freeze-out in high energy nuclear collisions”, Phys. Rev. Lett. 81 (1998) 5764-5767.

[22] U. Heinz, “The little bang: searching for quark-gluon matter in relativistic heavy-ion collisions”, Nucl. Phys. A685 (2001) 414c-431c.

[23] S. Scherer et al., “Critical review of quark gluon plasma signatures”, Prog. in Part. and Nucl. Phys. 42 (1999) 279-293.

[24] L.P. Csernai, “Introduction to relativistic heavy ion collisions”, John Wiley & Sons Ltd., West Sussex (1994).

[25] J. Rafelski, “Strangeness in quark-gluon plasma”, South Afr. J. Phys. 6 (1983) 37.

[26] J. Rafelski, and B. Muller, “Strangeness production in the quark-gluon plasma”, Phys. Rev. Lett. 48 (1982) 1066.

[27] J. Rafelski, and B. Muller, "Strangeness production and evolution in quark gluon plasma", Z.Phys. A324 (1986) 453-463.

[28] R. Koch et al., "Strangeness in relativistic heavy ion collisions", Phys. Rep. 142 (1986) 167.

[29] J.P. Blaizot, and A.H. Mueller, "The early stage of ultra-relativistic heavy ion collisions", Nucl. Phys. B289 (1987) 847-860.

[30] K.J. Eskola, K. Kajantie, and K. Tuominen, "Centrality dependence of multiplicities in ultrarelativistic nuclear collisions", Phys. Lett. B 497 (2001) 39-43.

[31] A. Krasnitz, and R. Venugopalan, "Initial gluon multiplicity in heavy-ion collisions", Phys. Rev. Lett. 86 (2001) 1717-1720.

[32] D. Kharzeev, and M. Nardi, "Hadron production in nuclear collisions at RHIC and high-density QCD", Phys. Lett. B 507 (2001) 121-128.

[33] A. Krasnitz, Y. Nara, and R. Venugolapan, "Coherent gluon production in very high energy heavy ion collisions", Phys. Rev. Lett. 87 (2001) 192302.

[34] L. McLerran, and J. Schaffner-Bielich, "Intrinsic broadening of the tranverse momentum spectra in ultrarelativistic heavy-ion collisions?", Phys. Lett. B 514 (2001) 29-32.

[35] L. McLerran, and R. Venugopalan, "Gluon distribution function for very large nuclei at small tranverse momentum", Phys. Rev. D 49 (1994) 3352-3355.

[36] L. McLerran, and R. Venugopalan, "Green's function in the color field of a large nucleus", Phys. Rev. D 50 (1994) 2225-2233.

[37] Y.V. Kovchegov, "Non-abelian Weizsacker-Williams field and a two-dimensional effective color charge density for a very large nucleus", Phys. Rev. D 54 (1996) 5463-5469.

[38] Y.V. Kovchegov, and D.H. Rischke, "Classical gluon radiation in ultrarelativistic nucleus-nucleus collisions", Phys. Rev. C 56 (1997) 1084-1094.

[39] M. Gyulassy, and L. McLerran, "Yang-Mills radiation in ultrarelativistic nuclear collisions", Phys. Rev. C 56 (1997) 2219-2228.

[40] L. McLerran, and R. Venugopalan, "Fock space distributions, structure functions, higher twists, and small x", Phys. Rev. D 59 (1999) 094002.

[41] A.H. Mueller, "Parton saturation at small x and in large nuclei", Nucl. Phys. B 558 (1999) 285-303.

[42] A.H. Mueller, "Small-x physics, high parton densities and parton saturation in QCD", hep-ph 9911289.

[43] A.H. Mueller, "Parton saturation-an overview", hep-ph 0111244.

[44] L. McLerran, and R. Venugopalan, "Computing quark and gluon distribution functions for very large nuclei", Phys. Rev. D 49 (1994) 2233-2241.

[45] J. Jalilian-Marian et al., "Intrinsic glue distribution at very small x", Phys. Rev. D 55 (1997) 5414-5428.

[46] E. Iancu, A. Leonidov, and L. McLerran, "Nonlinear gluon evolution in the color glass condensate: I", Nucl. Phys. A 692 (2001) 583-645.

[47] J.D. Jackson, "Classical Electrodynamics", Third Edition. Wiley, New York (1999).

[48] F. Wang, Ph.D. thesis, Columbia University (1996).

[49] T. Abbott et al. (E802 Collab.), "Comparison of p+A and Si+Au collisions at 14.6 GeV/c", Phys. Rev. Lett. 66 (1991) 1567.

[50] T. Abbott et al. (E802 Collab.), "Measurement of particle production in proton-induced reactions at 14.6 GeV/c", Phys. Rev. D 45 (1992) 3906.

[51] T. Abbott et al. (E802 Collab.), "Charged hadron distributions in central and peripheral Si+A collisions at 14.6 GeV/c", Phys. Rev. C 50 (1994) 1024.

[52] L. Ahle et al. (E866 Collab.), "Particle production at high baryon density in central Au+Au reactions at 11.6A GeV/c", Phys. Rev. C 57 (1998) 466.

[53] L. Ahle et al. (E866 Collab.), and B.B.Back et al. (E917 Collab.), "An excitation function of K^- and K^+ production in Au+Au reactions at the AGS", Phys. Lett. B 490 (2000) 53.

[54] F. Sikler et al. (NA49 Collab.), "Hadron production in nuclear collisions from the NA49 experiment at 158-GeV/c/A", Nucl. Phys. A661 (1999) 45c.

[55] C. Hohne et al. (NA49 Collab.), "Strangeness production in nuclear collisions: recent results from experiment NA49", Nucl. Phys. A661 (1999) 485c.

[56] I.G. Bearden et al. (NA44 Collab.), "Strange meson enhancement in Pb+Pb collisions", Phys. Lett. B471 (1999) 6.

[57] C. Adler et al. (STAR Collab.), "Multiplicity distribution and spectra of negatively charged hadrons in Au+Au collisions at $\sqrt{s} = 130$ GeV", Phys. Rev. Lett. 87 (2001) 112303.

[58] W. Deng, Ph.D. thesis, Kent State University (2002).

[59] C. Adler et al. (STAR Collab.), "Measurement of inclusive antiprotons from Au+Au collisions at $\sqrt{s} = 130$ GeV", Phys. Rev. Lett. 87 (2001) 262302.

[60] C. Adler et al. (STAR Collab.), "Mid-rapidity phi production in Au+Au collisions at $\sqrt{s} = 130$ GeV", Phys. Rev. C 65 (2002) 041901(R).

[61] I.G. Bearden et al. (NA44 Collab.), "Collective expansion in high energy heavy ion collisions", Phys. Rev. Lett. 78 (1997) 2080.

[62] N. Xu, and M. Kaneta, "Hadron freeze-out conditions in high energy nuclear collisions", Nucl. Phys. A698 (2002) 306-313.

[63] M. Calderon de la Barca, Ph.D. thesis, Yale University (2001).

[64] C. Adler et al. (STAR Collab.), "Results from the STAR experiment", Nucl. Phys. A698 (2002) 64c-77c.

[65] B.B. Back et al. (PHOBOS Collab.), "Ratios of charged antiparticles-to-particles near mid-rapidity in Au+Au collisions at $\sqrt{s} = 130$ GeV", Phys. Rev. Lett. 87 (2001) 102301.

[66] J.L. Bailly et al. (NA27 Collab.), "Strangeness and diquark suppression factors in 360 GeV/c p p interactions", Phys. Lett. B 195 (1987) 609.

[67] A.M. Rossi et al., "Experimental study of energy dependence in proton-proton inclusive reactions", Nucl. Phys. B 84 (1975) 269.

[68] T. Alexopoulos et al., "Mass-identified particle production in proton-antiproton collisions at $\sqrt{s}$= 300, 540, 1000, and 1800 GeV", Phys. Rev. D 48 (1993) 984.

[69] F. Wang, "Correlation between the charged kaon ratio and the baryon phase-space density in heavy-ion collisions", Phys. Lett. B 489 (2000) 273.

[70] F. Wang et al., "Systematic study of the kaon to pion multiplicity ratio in heavy-ion collisions", Phys. Rev. C 61 (2000) 064904.

[71] F. Wang, and N. Xu, "Baryon phase-space density in heavy-ion collisions", Phys. Rev. C 61 (2000) 021904(R).

[72] J.C. Dunlop, and C.A. Ogilvie, "Comparison of strangeness production between A+A and p+p reactions from 2 to 160 A GeV", Phys. Rev. C 61 (2000) 031901(R).

[73] P. Braun-Munzinger et al., "Maximum relative strangeness content in heavy ion collisions around 30-GeV/A", Nucl. Phys. A697 (2002) 902.

[74] L. Ahle et al. (E866 Collab.), "Kaon production in Au+Au collisions at 11.6A GeV/c", Phys. Rev. C 58 (1998) 3523.

[75] L. Ahle et al. (E866 Collab.), "Centrality dependence of kaon yields in Si+A and Au+Au collisions at relativistic energies", Phys. Rev. C 60 (1999) 044904.

[76] H. Boggild. et al. (NA44 Collab.), "Charged kaon and pion production at midrapidity in proton-nucleus and sulphur-nucleus collisions", Phys. Rev. C 59 (1999) 328.

[77] F. Wang, "Systematic of mid-rapidity K^{-}/π ratio in heavy-ion collisions", nucl-ex 0201018.

VITA

VITA

Alex Cardenas was born December 13th 1973 in Panama City, Republic of Panama. He graduated with high distinctions from Worcester Polytechnic Institute in May 1996 where he obtained a Bachelor of Science degree in Physics. He also worked as a grader at WPI from 1995 until 1996. In May 1998, he obtained his Master of Science degree in Physics from Purdue University. He served as a teaching assistant at Purdue University from 1996 through 1999, and as a research assistant from 1999 through 2002. He received his Ph.D. in experimental high energy nuclear physics from Purdue University in August 2002. His dissertation was one of the first from data obtained at Brookhaven National Laboratory's Relativistic Heavy Ion Collider. It is titled "Charged Kaon Production At Mid-Rapidity In Gold-Gold Collisions At 130 GeV".